Calibration of the ALICE Photon Spectromter (PHOS) using the $\pi^0 \rightarrow \gamma\gamma$ decay

Master Degree Thesis in Experimental Heavy Ion Physics

Henrik Qvigstad

Department of Physics and Technology
University of Bergen
Norway

September 2009

Acknowledgements

I would like to thank all those that contributed to this dissertation and those who supported me during the process of writing it. Foremost, I would like to thank my adviser, Prof. Joakim Nystrand, for all the help and advice he has given me these last couple of years. In addition, I would like to thank Prof. Dieter Röhrich in a similar vain. His help and advice has also been invaluable.

Furthermore, I would like to thank Boris Wagner, Per Thomas Hille, Matthias Richter, Artursz Szostak, Dag Larsen, Gaute Øvrebekk, Kenneth Aamodt, Johan Alme, Ketil Røed, Kalliopi Kanaki, Håvard Helstrup, Yuri Kharlov, Boris Polishchuk, and Joseph Young for taking the time to answer my questions, for allowing me to test my ideas on them, and for all the help and support they have given me. This goes especially for Øystein Djuvsland whom has been a constant source of both help and advice.

I would also like to thank those who I have studied and worked with these last 5 years, especially Kyrre Skjerdal, Magne Aanes, Sigurd Askeland, Sveinung Fjær, and Trond Helge Rolland for making it so much fun.

Lastly, I would like to thank my friends and family for supporting me through the experience. I could not have done this without all of you. A special thanks goes to Tone Magerholm for all her infinite support, understanding and late dinners.

-Henrik Qvigstad

Contents

Chapter 1

Introduction

Nuclear physics is the study of atomic nuclei and nuclear matter in general. Nuclear matter is a system of interacting nucleons or quarks, and is believed to form several distinct phases depending on its temperature and energy density. However, the specifics of these phases have not yet been fully established.

Historically, the main source of observation in nuclear physics has been radioactive decay. Particle accelerators capable of colliding particles at the nuclear scale have added insight into a larger range of interactions and phenomena.

Today, these accelerators are capable of colliding protons with other protons at a scale of several Giga–electron–Volt (GeV) at center of mass. The highest center of mass energy achieved in a proton - anti–proton (p–$\bar{p}$) accelerator is 1.96 TeV at the Fermilab Tevatron. However, p–$\bar{p}$ collisions are considered to be within the field of particle physics, a field that evolved out of nuclear physics. Today, high energy nuclear physics is focused on collisions between heavier nuclei. The highest center of mass energy achieved in a nucleus–nucleus collider is 100 GeV per nucleon at the Relativistic Heavy Ion Collider (RHIC) using gold (Au) nuclei.

The Large Hadron Collider (LHC) is under construction beneath the border between Switzerland and France. If it is successful, it will accelerate and collide protons at 7 TeV per proton in center of mass. Furthermore, it will collide lead (Pb) nuclei at 2.76 TeV per nucleon. These energies will contribute to the understanding of nuclear matter.

There are different theories explaining how nuclear matter will behave at these energies. Most of them consider nuclear matter to undergo phase changes, analogous to a thermodynamical medium. The RHIC experiment, and experiments with fixed targets at CERN, showed indications that nuclear matter might be approaching a sort of Quantum Chromo–Dynamics (QCD) phase change around a temperature of $\sim$ 175 MeV. In this new phase, conventionally called Quark–Gluon Plasma (QGP), quarks may be

deconfined from hadron structures.

The LHC will produce collisions where the energy density reaches levels where numerical calculations predicts QGP using a method called Lattice QCD. However, this must be a short lived state as the collision will immediately expand with a speed close to the speed of light. It is therefore not clear if the collisions reach significant equilibrium for QGP to form before the nuclear matter expands to lower densities.

A high energy nuclear collision produces significantly large amounts of photons. A large part of these photons are the result of decay of other particles, such as the decay from a π^0 into two photons. Direct Photons are photons that are not the result of decay of other particles. Such photons may stem from partonic interactions, in particular Compton scattering between a gluon and a quark $g + q \rightarrow \gamma + q$. Furthermore, if QGP is formed then it may emit photons collectively as a thermal medium. A large amount of information about nuclear matter is contained within the spectra of these nuclear collision photons. However, a high precision spectra is needed in order to decouple the statistics of the different processes.

Several experiments are being built along the beam of LHC. Among these are ALICE. ALICE is a detector experiment dedicated to heavy ion physics. It will have two electro–magnetic calorimeters. One of these, the PHOton Spectrometer (PHOS), will provide high precision coverage at mid–rapidity in about 1/3 of the full azimuthal angle. However, PHOS needs to be calibrated before it can yield an accurate photon spectra.

In this thesis we will present calibration techniques proposed for calibrating PHOS. We will go into the details of one of these techniques, calibration using neutral pions (π^0). Furthermore, we will present an implementation of this technique and the result of the implementation used on simulated data. Lastly, we will attempt to evaluate the techniques effectiveness.

1.1 The Standard Model

The Standard Model is a generally accepted theory describing the elementary particles and their interaction. It is based on relativistic quantum field theory. Therefore, it is consistent with quantum mechanics and the special theory of relativity.

To this date, most of its experimental predictions have been empirically verified. The only particle predicted by the Standard Model not yet observed is the Higgs Boson. The existence of the Higgs Boson will be tested in experiments at LHC. However, the Standard Model is not a complete model of elementary physics. For example, it does not explain gravitation.

1.1.1 Elementary Particles

The SM is a grouping of two theories, the electro–weak theory and quantum chromodynamics. In the two theories, the elementary particles are the leptons and the quarks.

An elementary particle has electro–magnetic charge, zero in cases of the neutrinos, and a particle and its anti–particle have opposite charge. Table 1.1 shows an overview of the particles[1].

All elementary particles are fermions. Fermions are particles that obey Fermi–Dirac statistics. They have half–integer spin(relative to bosons integer spin), and no two fermions can occupy the same state at the same time. There are three families of leptons and quarks. Furthermore, each family consists of two types of particles, and each of these particle has an anti–particle.

Fermion	**Family**	**EM Charge**
Lepton	$\nu_e \quad \nu_\mu \quad \nu_\tau$	0
	$e \quad \mu \quad \tau$	-1
Quark	$u \quad c \quad t$	$+2/3$
	$d \quad s \quad b$	$-1/3$

Table 1.1: Elementary particles, fermions. The corresponding anti-particles are not listed. e.g. the positron (e^+). The EM charges are expressed as fractions of the elementary charge e.

The elementary interactions are meditated by gauge bosons. The photon carries the electro–magnetic force, and is mass–less. The $W^\pm$ and the Z^0 carry the weak force, and have a relatively large mass, ~ 80 and ~ 91 GeV. Last is the gluon which carries the strong force. It is, if not mass–less, of very low mass.

All gauge bosons are, ironically, bosons. Bosons are particles that obey Bose-–Einstein statistics. They have integer spin(relative to fermion half–integer spin). There is no limit to the amount of bosons that can occupy the same state at the same time.

Table 1.2 shows an overview of the gauge bosons[1].

Interaction		**Particle**
Strong		gluon (g)
Electro-Weak	EM	γ
	Weak	$W^\pm$, Z^0

Table 1.2: Gauge bosons. The particles through which the elementery particles interact.

1.1.2 Composite Particles

Elementary particles in nature are often grouped together in quantum mechanical states. Quarks, bound by gluons, group together to form protons and neutrons. Protons and neutrons group together to form atomic cores. These atomic cores attract electrons, and they group to form atoms. Atoms group together in molecular structures and form, in large numbers, matter as we know it.

There are more exotic combinations of particles. Quarks and gluons generally group together in hadrons. Protons and neutrons are the most common hadron as they are stable. Hadrons are combinations of two or three quarks, i.e. mesons or baryons. However, quarks can group together in more complex structures, such as Quark Gluon Plasma (QGP.) Generally, all these structures are called nuclear matter. Quarks never appear as free particles. We observe them only as hadrons in detectors.

1.1.3 QCD - Quantum ChromoDynamics

Quantum ChromoDynamics is the theory of strong interaction, the interaction between quarks and gluons. Analogously to electric charge, a quark has a QCD charge. However, in QCD there are 3 independent charges, i.e. 3 independent quantum numbers, called *colour charge*. Individually they are named red, green and blue. However, the naming does not have any relation to colour in the visual sense, i.g. the flower is red. The choice of name is completely arbitrary, but in this case it has become convention.

According to Coulomb's law, the force between two electrically charged particles converges at infinite distance and diverges at zero distance. According to the theory of Asymptotic Freedom and its product Confinement, the force between two colour charged particles behaves quite opposite to that of EM charged particles[2, 3]. The force converges at zero distance, and it diverges at infinite distance. Thus, colour charged particles at close distance are virtually non–interacting, and separating two colour charged particles would require infinite energy.

Every charge has a corresponding anti–charge (e.g. anti–red). Combinations of charges that are neutral are called white. Such a white charge can for example be the product of *red* + *anti-red* or *red* + *green* + *blue*. Since a free QCD article must be white, a single quark cannot be free.

Bound state of quarks are necessarily composite particles. These states are observed as a combination of two or three quarks, hadrons. There are two types of hadrons. They are the mesons and baryons. A meson is a state of two quarks, a bosons, and not stable. The most common type of meson in nuclear collisions are the pions. They are combinations of *up*, *down*, *anti-up* and *anti-down* quarks.

A baryon is a state of three quarks and is a fermion. Two of theses

baryons, protons and neutrons, are the basic constituents of a nucleus. A atomic nucleus is a state of protons and neutrons held together by the strong force. For example, the lead nucleus has 82 protons and 125 neutrons.

1.2 Quark-Gluon Plasma

In normal nuclear matter, the protons and the neutrons are bound to each other in atomic nuclei, and the quarks are again bound to their respective protons and neutrons. With the exception of radioactive decay, the nuclear states do not change.

If the density and/or energy density/temperature is increased significantly, as in an heavy ion collision, then the nucleus scructure breaks down. In the initial collision, hard scattering between partons[1] occur, and exotic quarks may be created. However, in the nuclear phase that follows the partons are still largely bound to hadrons. Because hadrons in this state are not bound to structures such as atom nuclei, they behave similarly to free atoms in a gas. Therefore, this phase of nuclear matter is called hadronic gas. In figure 1.1, this phase is depicted as area which is labeled Hadrons.

If the density and/or energy density is increased further, then it is possible that the hadron structure breaks down. As quarks are colour charged, they may not be free. However, if the energy density and/or density becomes high enough, the colour charge may be screened, and the quarks are no longer confined to hadrons. This state of nuclear matter is called "Quark Gluon Plasma"(QGP), and is depicted as area which is labeled "Quarks and Gluons" in figure 1.1.

It is thought that the universe started with a Big Bang, an explosive expansion from a point. During a early part of this expansion, the energy density and density would be high enough for QGP to form. Creation of QGP can therefore be viewed as recreation of conditions of the early universe. In addition, it is possible that neutron stars contain deconfined states of quarks. If so, it is a result of the stars extreme density.

Lattice QCD is QCD formulated on a space-time lattice. It is discrete formulation which allows numerical solutions to be found. It has been used to describe the theoretical phase transition to QGP.

1.3 Results from the Relativistic Heavy Ion Collider

The Relativistic Heavy Ion Collider (RHIC) is an accelerator built for heavy ion experiments by Brookhaven National Laboratory (BNL). RHIC has run

[1]Parton is an alternative name for the constituents of hadrons, i.e. quarks and gluons.

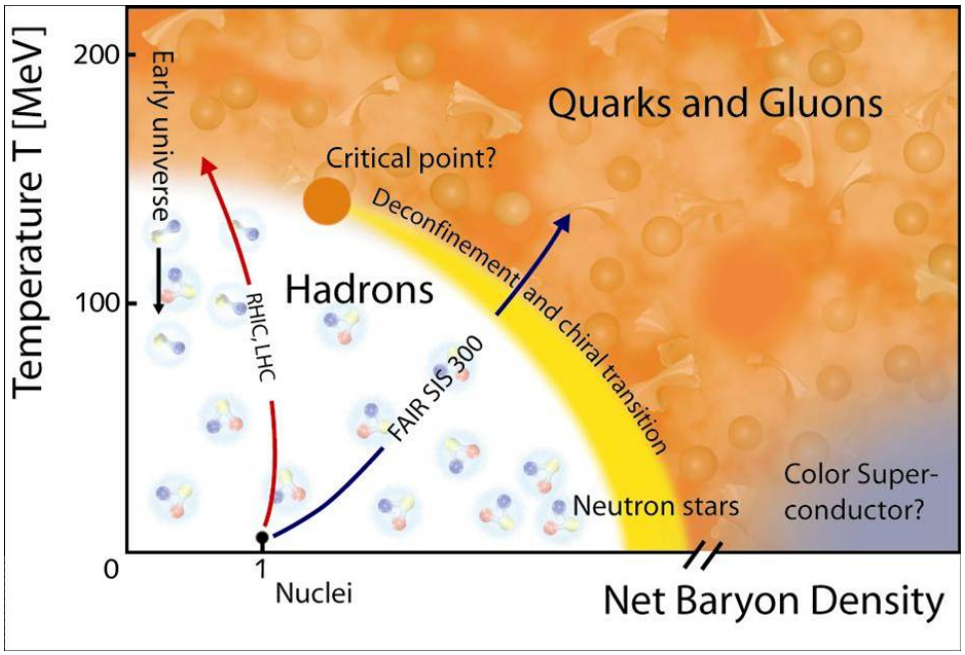

Figure 1.1: Nuclear Phase Diagram. Shows the different states of nuclear matter on a plane of density and temperature. From [4]

p–p, d–Au (deuteron–Gold), Cu–Cu (Copper), and Au–Au collisions at energies up to 100 GeV per nucleon. The RHIC experiments have produced evidence of strongly coupled deconfined state of matter. Some of the most interesting observations from these collisions will be summorized below.

1.3.1 Jet Suppression

As a quark is colour charged, it cannot exist in a free state. However, a high energy quark may break away from the colour charges neutralising it by creating a quark anti–quark pair. This process will occurs untill no state of quarks has the internal energy to create further pairs.

Jets are the products of quark–quark, quark–gluon, and gluon–gluon, scatterings in hadronic collisions. These scatterings produce two outgoing quarks and/or gluons, both of whom cause jets. In their rest frame, they are emitted back–to–back. We observe such quark–quark scatterings as back–to–back correlations in the transverse plane.

If we now define the azimuthal angle[2] of the highest momentum hadron in a jet event to be $\phi = 0$ and study the azimuthal distribution of high–momentum particles relative to ϕ, $\Delta\phi$. Then, RHIC experiments show a sharp peak in hadron multiplicity centered in forward direction ($\Delta\phi = 0$) for

[2]See section 1.4.

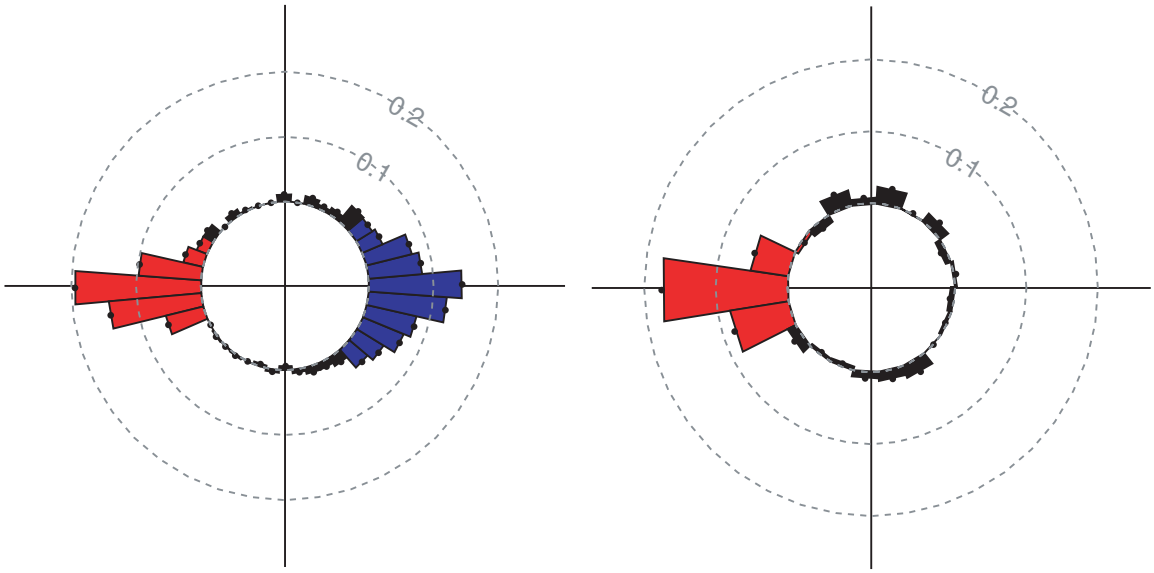

Figure 1.2: Results from STAR, at RHIC. The azimuthal distribution of multiplicity for unidentified hadrons above tranverse momentum $p_T > 2\ GeV$ for proton–proton (left) and background subtracted central gold–gold collisions (right). The angle in the plot is the relative azimuthal angle $\Delta\phi$, relative to angle ($\phi = 0$) of the highest tranverse momenta particle. We will define p_t and ϕ in section 1.4. From [5].

p–p, deuteron–Au and Au–Au collisions. This is due to other hadrons fragmenting from the same parton as the highest momentum hadron. Furthermore, the experiments show a wider peak near backwards direction ($\Delta\phi = \pi$) for p–p and d–Au.

However, for Au–Au the backward multiplicity disappears, or is smudged out to larger angles, as shown in figure 1.2. This is called jet suppression and is seen as an effect of the backward scattered quark passing through hot QCD matter. This hot QCD matter slows down the quark through colour charge Bremsstrahlung[3], and this leads to a decreased and/or smudged backward jet [5].

1.3.2 Thermal Photons

The search of thermal photons at RHIC have not provided conclusive results. At low p_T, where there is very low precision, we can only make a qualitative statement that thermal photons or something similar, which we can more generally call soft photons, are probably present[6]. This is a statement based on the assumption that anything perturbative QCD does not predict

[3] see section 1.5.3

would belong to the thermal/soft category.

1.3.3 Flow - v_2

Particles emitted from heavy ion collisions at RHIC show a collective effect referred to as flow. The initial state immediately following a collision is characterised by extremely high densities, and if there are large interaction cross sections between the constituents then density gradients are expected to translate to pressure.

In non–central nuclear collisions, the nuclear overlap region is not circular in the transverse plane, but it is instead roughly elliptically shaped, and the initial density gradients should not be isotropic. Then, as the system evolves in time, the spatial distribution should becomes more isotropic as the participants collectively expand, but the momentum distribution created by the initial anisotropic pressure is preserved through the evolution to the finally observed hadron distributions.

Experimentally, flow is measured as a dependency on the azimuthal angle (ϕ), of particles relative to the reaction plane[4]. Using a Fourier decomposition, the flow can be parametrized as v_2:

$$\frac{dN}{p_T dp_T dy d\phi}(p_T, y, \phi; b) = \frac{dN}{p_T dp_T dy}[1 + 2v_2(p_T, y; b)cos(2\phi) + \dots] \quad (1.1)$$

Figure 1.3 show v_2 as a function of p_t for different identified hadron species. The difference in v_2 for various particle types, in particular between baryons and mesons, can be explained by models that assume that hadrons are formed through quark coalescence. However, measurements from the PHOBOS experiment indicates that v_2 drops as one moves away from mid-rapidity[5].

1.3.4 Direct Photons

Direct photons are photons emitted directly from the collision and not the result of the decay of other particles. They can be produced in partonic interactions. For example by the Compton–like process $g + q \rightarrow \gamma + q$.

The PHENIX experiment has measured the yield of direct photons at mid-rapidity for $p_T = 5 - 16\ GeV$. Because the production of high energy photons occur primarily in the initial phase of the collision, the yield of direct photons can be compared to the yield from p–p collision scaled by incident parton flux of the Au–Au over that of the p–p flux. This is called binary collision scaling. The data show that the measured direct–photon yield agrees very well with this expectation[5]. This is taken as evidence that emitted photons pass through the medium unaffected.

[4] see section 1.4 and figure 1.4

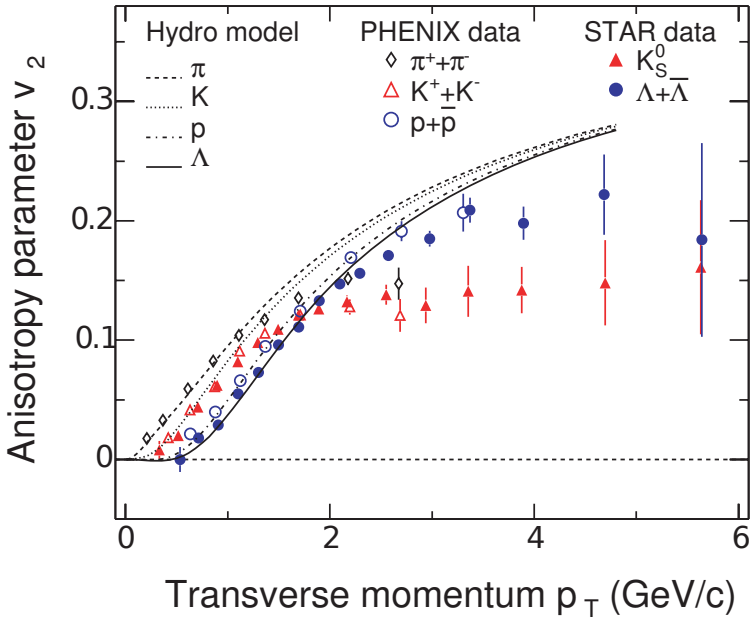

Figure 1.3: Results from PHENIX and STAR, at RHIC. Azimuthal anisotropy (v_2) as a function of p_T from minimum bias gold-gold collisions. Hydrodynamic calculations are indicated by dashed lines. From [5].

1.4 Kinematics of high energy nuclear collisions

The momentum of a particle emitted from an high–energy nucleus–nucleus collision can be described by its 3 momentum components p_x, p_y, and p_z. The z–direction is by convention chosen as the direction of the beam. However, there are 3 different kinematic variables commonly used in heavy ion and particle physics. These are the rapidity (y), the transverse mass (m_T), and azimuthal angle (ϕ).

The transverse mass (m_T) of a particle is defined as:

$$m_T^2 = p_T^2 + m^2 \tag{1.2}$$

where the transverse momentum (p_T) is the component of the momentum that is orthogonal to the beam direction, m is the mass of the particle, and we are using units where the speed of light is $c = 1$. We will use units where $c = 1$ from now on.

Azimuthal angle (ϕ) is the angle of the particles momentum in a plane orthogonal to the beam direction.

The rapidity (y) of a particle is defined as:

$$y = \frac{1}{2} ln \left[\frac{E + p_L}{E - p_L} \right] \tag{1.3}$$

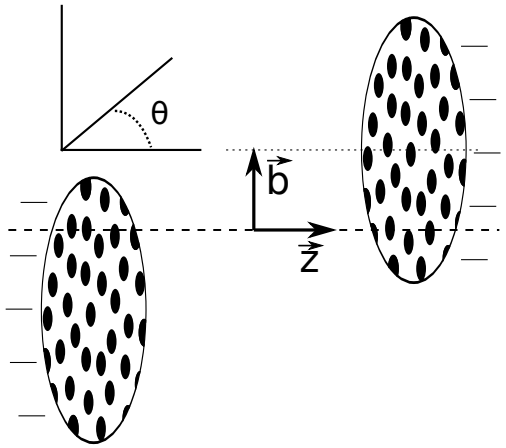

Figure 1.4: A sketch showing often used collision parameters and coordinates: $\vec{z}$ - beam direction, $\vec{b}$ - impact parameter, and θ - angle to beam direction. The event plane is spanned by the $\vec{z}$ and $\vec{b}$. The azimuthal angle (ϕ) is the angle in the transverse plane, the plane orthogonal to the beam direction.

where p_L is component of the momentum that is parallel to the beam direction. A important quality of rapidity is that the relative rapidity between two particles is independent of Lorentz boost along the beam direction.

1.4.1 Pseudo–Rapidity - η

Pseudo–rapidity is a coordinate describing the angle of a particle relative to the beam axis. In terms of angle to the beam axis (θ) it is defined as:

$$\eta = -ln\left[tan(\frac{\theta}{2})\right] \tag{1.4}$$

In terms of the particles momentum ($\vec{p}$) it is:

$$\eta = \frac{1}{2}ln\left[\frac{|\vec{p}| + p_L}{|\vec{p}| - p_L}\right] \tag{1.5}$$

where p_L is the momentum component of the particle parallel to the beam axis. In the case where $m \ll |\vec{p}|$, pseudo–rapidity is approximately equal to rapidity, eq. 1.3.

1.4.2 The Neutral Pion - π^0

Pion ($\pi^{+/-/0}$) is the name of a group of mesons, consisting of up and down quarks. Pions are the lightest mesons, and have an high production cross

section in nuclear collisions. About $80 - 90$ % of the particles produced in the collision are pions.

The neutral pion (π^0) is one of these pions. It has a very short life time ($\tau = 8.4 \pm 0.6 \times 10^{-17}$ s) which causes it to decay very close to the interaction point (IP), at an average of $\simeq 25\beta\gamma$ nm from the IP. It decays to two photons ($\pi^0 \rightarrow \gamma\gamma$) with a probability of 98.8%. Due to the short decay time, the gammas are emitted approximately from the IP. It has a mass of 134.98 MeV[1].

1.4.3 Invariant mass

According to the theory of relativity, a particles mass is invariant in all frames of reference. A relativistic particle can be described by a four–vector, a vector in the four-dimensional real vector space called Minkowski space:

$$p^\mu = (E, \vec{p}) \tag{1.6}$$
$$p_\mu = (E, -\vec{p}) \tag{1.7}$$

The inner product of such a four–vector with itself is the mass of the particle squared:

$$p^2 = p^\mu p_\mu = E^2 - \vec{p}^2 = m^2 \tag{1.8}$$

Furthermore, if a particle decays into two other particles then the four-vector inner product must be conserved. Consider a $\pi^0 \rightarrow \gamma\gamma'$ decay. The inner product of the π^0 four–vector with itself is its mass, ~ 135 MeV.

$$p_{\pi^0}^2 = m_{\pi^0}^2 \tag{1.9}$$

The inner product of the sum of the two photons with itself must be equal to the inner product of the π^0 with itself.

$$p_{\pi^0}^2 = (p_\gamma + p_{\gamma'})^2 \tag{1.10}$$

Combining eq. 1.9, eq. 1.10, and eq. 1.8 gives

$$m_{\pi^0}^2 = (p_\gamma + p_{\gamma'})^2 = (E_\gamma + E_{\gamma'})^2 - (\vec{p}_\gamma + \vec{p}_{\gamma'})^2 \tag{1.11}$$

Another form of the above equation is:

$$m_{\pi^0}^2 = 2E_\gamma E_{\gamma'}(1 - cos(\Psi)) \tag{1.12}$$

where Ψ is the opening angle between the two photons. Here we have used the fact that $E = |\vec{p}|$ in the case of mass less particles.

1.5 Passage of Charged Particles Through Matter

When a charged particle passes through matter, reactions with the atoms or nuclei as a whole or with their individual constituents may occur; depending on the particle, its energy, and the type of material. This occurs with a probability governed by the laws of quantum mechanics and the relative strength of the basic interactions involved. For charged particles and photons, the most common processes are electromagnetic interactions [7].

1.5.1 Energy Loss of (Heavy) Charged Particles

In general, two principal features characterize passage of charged particles through matter: A loss of energy by the particle and a deflection of the particle from its incident direction. They are primarily the result of two processes:

1. Inelastic collision with the atoms in the material that leads to excitation and/or ionization.

2. Elastic scattering from nuclei.

Both occur many times per unit path length in matter, and it is their cumulative result which accounts for the two principal effects observed. However, other processes may occur, and include:

- Cerenkov radiation
- Nuclear reactions
- Bremsstrahlung

Bethe–Bloch

The Bethe–Bloch formula is the basic expression for calculating the energy loss per distance of a swift, heavy (relative to the electron), charged particle. It is expressed below, with two normally applied corrections: the *density effect correction* δ and the *shell correction* C,

$$-\frac{dE}{dx} = 2\pi N_a r_e^2 m_e c^2 \rho \frac{Z}{A}\frac{z^2}{\beta^2}\left[ln\left(\frac{2m_e\gamma^2 v^2 W_{max}}{I^2}\right) - 2\beta^2 - \delta - 2\frac{C}{Z}\right] \quad (1.13)$$

1.5.2 Minimum Ionising Particles - MIP

As seen in figure 1.5, the minimum value of $\frac{dE}{dx}$ is almost at the same particle energy for all materials. Particles at this point are know as minimum

N_a:	Avogadro's number	β:	v/c of particle
r_e:	classical electron radius	γ:	$1/\sqrt{1-\beta^2}$
m_e:	electron mass	W_{max}:	maximum energy transfer in a single collision
ρ:	density of absorbing material		
Z:	atomic number of absorbing material	I:	mean excitation potential
A:	atomic weight of absorbing material	δ:	density correction
z:	particle charge	C:	shell correction

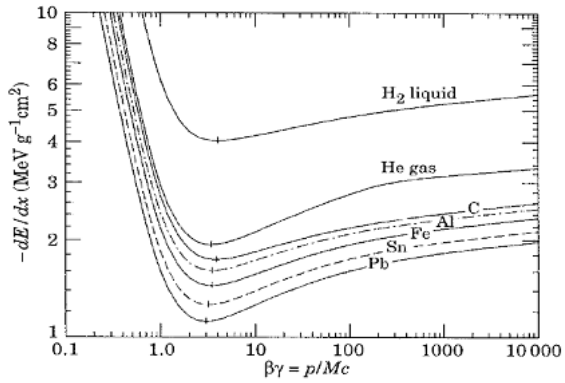

Figure 1.5: Bethe-Bloch solved for a set of materials. Taken from [8].

ionizing. Beyond this point, the energy loss per distance increases slowly. This continues until Bremsstrahlung takes effect.

Particles with charge $c = \pm e^{\pm}$, and energy in the minimal ionizing range, are often referred to as Minimum Ionizing Particles (MIP). They deposit energy per distance with a small statistical variance only weakly dependent on particle momentum.

1.5.3 Bremsstrahlung

Bremsstrahlung is the emission of electromagnetic radiation arising from scattering in the electric field of a nucleus from a particle transversing matter. For electrons at small energies, a few MeV or less, this process is a small factor. However, as the energy increases the probability of Bremsstrahlung increases so that at a few 10's of MeV, loss of energy by radiation is comparable to or greater then the collision ionization loss. For other charged particles, this is most often a negligible process due to their high mass[7].

1.5.4 Critical energy - E_c

The critical energy of a material is defined as the energy of an electron transversing the material where energy loss via radiation equals radiation

loss via collisions:

$$E_c \; \epsilon \; \left(\frac{dE}{dx}\right)_{rad} = \left(\frac{dE}{dx}\right)_{coll} \tag{1.14}$$

Material	Critical energy [MeV]
Pb	9.51
Al	51.0
Fe	27.4
H_2O	92

Table 1.3: Critical energies of some material. Taken from [7].

1.5.5 Radiation length

The radiation length of a material is defined as the length over which the electron energy is reduced by a factor $1/e$. Radiation length is also very similar to mean free path (λ_{pair}) of a γ–ray for pair production. They are related as stated in equation 1.15

$$\lambda_{pair} \simeq \frac{9}{7} L_{rad} \tag{1.15}$$

Material	$[gm/cm^2]$	$[cm]$
Pb	6.37	0.56
Al	24.01	8.9
Fe	13.84	1.76
H_2O	36.08	36.1

Table 1.4: Radiation length of some material. From [7].

1.5.6 Pair production

Pair production is the process through which a photon (γ) is transformed to an electron (e^-), positron (e^+) pair , $\gamma \rightarrow e^+e^-$. Pair production requires a photon with at least $1.022MeV$ of energy and a third body, usually a nucleus. Pair production occurs approximately with a mean free path given by equation 1.15.

1.5.7 Electro–Magnetic Shower

An electro–magnetic shower or electron–photon shower is the process through which high energy electrons and photons deposit their energy in a dense material. It is the result of two processes:

- Pair production ($\gamma \rightarrow e^+e^-$)
- Bremsstrahlung emission ($e^{\pm} \rightarrow e^{\pm}\gamma$)

A high energy photon in matter converts into an electron and a positron pair which then emit energetic Bremsstrahlung photons. These, in turn, convert into further e^+e^- pairs, and so on.

Simulations show that beyond the first radiation length or so, the energy loss ($\frac{dE}{dz}$) can be fitted reasonably well by the gamma distribution[7]:

$$\frac{dE}{dz} = E_0 b \frac{(bz)^{a-1}e^{-bz}}{\Gamma(a)} \tag{1.16}$$

where a and b are parameters dependent on the material. The maximum penetration depth z_{max} is then given by,

$$z_{max} = \frac{a-1}{b} \tag{1.17}$$

The transverse dimensions of electromagnetic showers is most conveniently measured in terms of the Moliere Radius, given by:

$$R_M = L_{rad}\frac{E_s}{E_c} \tag{1.18}$$

where $E_s = m_e c^2\sqrt{4\pi/\alpha} = 21.2\ MeV$, L_{rad} is radiation length, and E_c is critical energy. Around 90% of a shower is contained within a radius of 2 R_M.

1.5.8 Scintillator

A scintillator is a material which emits light as a result of being struck by ionizing radiation. When coupled to an amplifying device such as a photomultiplier, the radiation can then be measured as the electric pulse of the photomultiplier. This pulse holds information about the energy deposited by the radiation. Such a setup is useful for measuring the energy deposited by an electromagnetic shower, but can used to measure energy deposited by other particles, such as charged pions[7].

Chapter 2

LHC And The ALICE Experiment

2.1 LHC

The Large Hadron Collider (LHC) is a large circular accelerator under construction beneath the border between Switzerland and France near Geneva. The accelerator is a project by the European Organization for Nuclear Research (CERN), or in french: the "Organisation Européen pour la Recherche Nucléaire." The LHC will be, at its completion, the largest accelerator in the world. It is roughly circular with a circumference of 27 km, and is placed underground at a depth of $\sim$100 m. It will accelerate, store, and collide protons and heavy ions, and the detectors along it will collect data. At present date, the first collision is expected at end of November 2009 according to schedule. The schedule also permits the possibility of lead ion collisions in 2010.

LHC will run p–p and Pb–Pb collisions:

- During nominal p–p runs, LHC will collide proton beams with a maximal center mass (CM) energy of $\sqrt{s} = 14\ TeV$ at luminosity $\mathcal{L} = 10^{34} cm^{-2} s^{-1}$. This type of run will take up most of the run-time for LHC. The collision energy during the first run is foreseen to be $\sqrt{s} = 7\ TeV$, and the luminosity somewhat lower then the design value. The very first collisions might actually occur at injection energy, i.e. $\sqrt{s} = 900\ GeV$.
- During Pb–Pb runs, LHC will collide at maximal CM of $\sqrt{s} = 5.5\ TeV$, and at luminosity $\mathcal{L} = 10^{27} cm^{-2} s^{-1}$. Pb–Pb runs will last for about 1 month an year.

Along the LHC, four detector are being built. They are:

- ALICE (A Large Ion Collider Experiment), optimized for Pb–Pb.

- ATLAS (A Toroidal LHC Apparatus), optimized for p–p.
- CMS (Compact Muon Solenoid), optimized for p–p.
- LHCb (LHC beauty), a specialized b–quark physics experiment.

In addition, there are two smaller experiments which focus on measurements in the very forward region. They are TOTEM, which shares its IP with CMS, and LHCf, which shares its IP with ATLAS.

2.2 ALICE - Overview

A Large Ion Collider Experiment (ALICE) is one of the six detector experiments being built along the LHC. It is optimized to study heavy ion collisions However, ALICE will also collect data from p–p events. This data will serve as a tool for calibration and as a source of reference.

With a nominal nucleon–nucleon CM energy at $\sqrt{s} = 5.5\ TeV$, the LHC will exceed RHIC energies, $\sqrt{s} = 200\ GeV$, which previously was the highest CM energy available. ALICE data should provide additional insight into the state of hot and dense nuclear matter. It should be able to test the existence of QGP and determine its properties. New phenomena is also expected, as such historically appear at such a large leap in energy.

ALICE was designed and built to handle a multiplicity of 8000 charged particles per unit rapidity at mid rapidity, $(dN_{ch}/d\eta)_{\eta=0} = 8000$, $N_{ch} = 84210$, which is above all predictions [9]. It was also a requirement of the detector to be able to track and identify particles from very low ($\sim$100 MeV) up to high ($\sim$100 GeV) transverse momenta (p_t). RHIC data has indicated that multiplicity might be in the lower range of predictions, around 3500 at maximum multiplicity[10].

2.3 ALICE - Layout and Sub–Detectors

In this section we will give a brief overview of the layout and the different sub–detectors of ALICE. More detailed information can be found in [9, 10]. As shown in figure 2.1, ALICE consists of a central detector system and several forward systems.

The central system is installed inside a large solenoidal magnet which generates a magnetic field of 0.5 T and covers a mid-rapidity range of $|\eta| \leq 0.9$ at CM. The central system includes, from the interaction vertex to the outside, six layers of high-resolution silicon detectors (ITS), the main tracking system of the experiment (TPC), a transition radiation detector for electron identification (TRD), and a particle identification array (TOF). The central system is complemented by three detectors without full

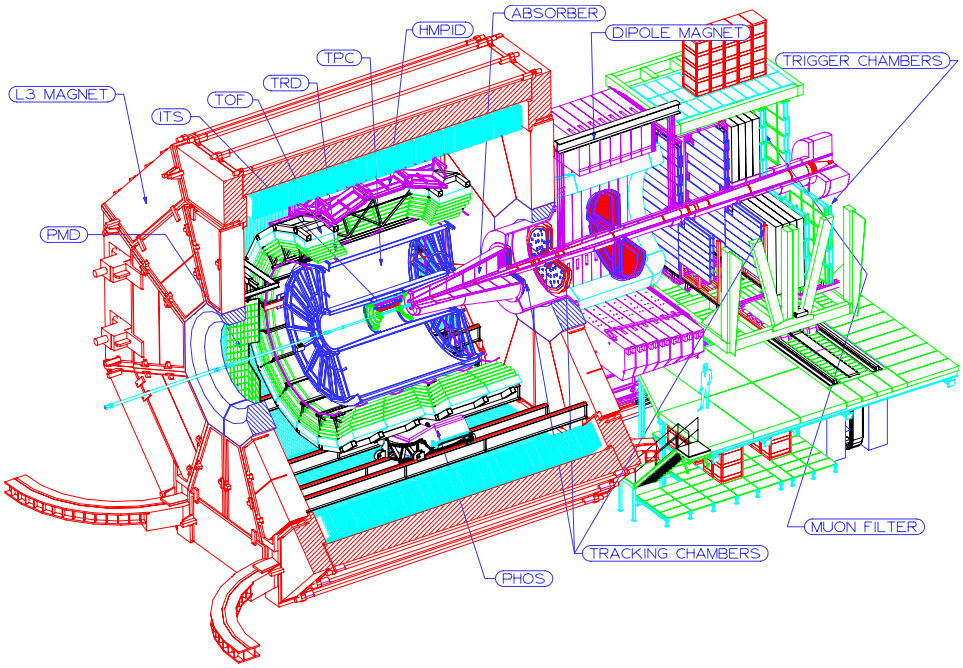

Figure 2.1: Diagram of the ALICE detector

coverage: a array of ring-imaging Cherenkov detectors (HMPID) and two electromagnetic calorimeter (EMCal & PHOS).

The forward systems consists on one side of a photon counting detector (PMD). On the other side there is an ensemble of multiplicity detectors (FMD); two sets of neutron and hadron calorimeters $\sim 120m$ down stream from the interaction point; and a muon spectrometer consisting of an absorber, a dipole magnet, five tracking stations, an iron wall (muon filter), and two trigger stations behind the muon filter. On each side there are also the V0 and T0 quartz counters that are used to determine vertex position and start–time[10].

2.3.1 Central Tracking Detectors

Tracking detectors track the path of charged particles. This is useful for determining vertex position and matching signals in other detectors, sutch as calorimeters and other tracking detectors, with the path of particles. In addition, if the tracking detector is in a magnetic field, then the curvature a charged particle's track can be used to determine its momentum.

The inner tracking detector of ALICE is a semiconductor based detector. More specifically, it is 6 layers of pixel, drift, and strip silicon detectors. The outer tracking detector of ALICE is a gas ionization based detector. More specifically, it is a Time Projection Chamber (TPC). For more information

regarding these kind of detectors see [7].

ITS - Inner Tracking System

ITS consists of six cylindrical layers of silicon detectors located at radii r = 4, 7, 15, 24, 39 and 44 cm. All its layers fully cover the rapidity range of $|\eta| < 0.9$, the same as TPC's rapidity range, while the inner most layer covers rapidity $|\eta| < 1.98$. The two innermost layers are silicon pixel detectors (SPD). The two following layers are silicon drift detectors (SDD), and the two outermost layers are silicon strip detectors (SSD). This choice is due to the decreasing granularity and cost of these types of detectors together with the decreasing track density. The ITS detectors are designed to have a resolution of the order of a few tens of μm, with the best precision in the innermost layer: 12 μm in $r\varphi$[10].

TPC - Time Projection Chamber

The TPC is the main tracking detector of the ALICE central barrel. Together with the other central barrel detectors, it must provide charged-particle momentum measurements with good two-track separation, particle identification, and vertex determination. It fully covers the rapidity range $|\eta| < 0.9$ or up to $|\eta| < 1.5$ for tracks with reduced track length. Together with the magnet, the detector has good momentum resolution up to $\sim 100\ GeV$. In addition, data from the central barrel detectors will be used to generate a fast on–line High-Level Trigger (HLT) for the selection of low cross-section signals.

The detector is made of a large cylindrical field cage, which has an inner radius of about 85 cm, an outer radius of about 250 cm, and an length along the beam direction of 500 cm. A high voltage membrane in the middle of the detector creates an electric field towards the detectors ends, which are covered with 560 000 readout pads. Charged particles moving through the detector will ionize the gas, Ne/CO_2. Due to the parallel electric and magnetic fields, the free ions and electrons will drift towards the membrane and the readout pads, respectively. The drift time, coupled with pad position, gives a measurement of all 3 space dimensions.

While measurements in two of the space dimensions are given by the pad positions, measurements of the third and time is both contained in the arrival time. Because events will overlap, especially in p–p, the time in which the particle causing ionization traversed the TPC may be that of several different events. This is solved by matching the track with the measurements of other detectors, e.g. the tracks in ITS.

2.3.2 Central Calorimeters

A calorimeter is a detector that measures the energy of particles. ALICE has two central calorimeters, and they are both electro–magnetic calorimeters. When an electron, positron, or photon enters a such a calorimeter, it initiates an electro–magnetic shower depositing all its energy in form of visible light and low energy electrons. However, deposition off all the energy of an EM shower requires that the calorimeter is big enough to contain the entire shower. This energy, in the form of light, is then measured by photo–diodes. For more details about EM showers and scintillators see section 1.5.7 and 1.5.8, For more information regarding these kind of detectors see [7].

EMCAL - Electro–Magnetic CALorimter

The EMCAL is a layered Pb-scintillator sampling calorimeter to be located inside the magnet of ALICE within a cylindrical integration volume approximately 112 cm deep in radial direction, and covers the rapidity of $|\eta| < 0.7$ within an azimuthal angle of $\Delta\varphi = 110^o$.

The EMCAL enhances ALICE's capabilities for jet quenching measurements. In addition, EMCAL enables triggering on high energy jets; reduces significantly the measurement bias for jet quenching studies; improves jet energy resolution; and augments existing ALICE capabilities to measure high momentum photons and electrons, with excellent resolution between 100 MeV/c and 100 GeV/c momenta [11].

PHOS - PHOton Spectrometer

PHOS is a low acceptance high granularity detector with high energy resolution. It is presented in detail in chapter 3.

2.3.3 Trigger System

The ALICE trigger is designed to select events displaying a variety of different features at rates which can be scaled down to suit physics requirements and the restrictions imposed by the bandwidth/capacity of the DAQ and the HLT. Read-Out triggering is controlled by a Central Trigger Processor (CTP). It communicates with the individual detectors inside ALICE via signals. The signals are divided into levels: L0, L1, and L2 [10].

L0 (Level 0) and L1 (Level 1) signals are emitted by detectors. They are separated into two levels as a result of the requirement of fast response and the need for information. L0 is a short signal sent to CTP within 0.8 μs, and its purpose is to inform the CTP that the detector has observed the characteristics of an event. After receiving the L0, the CTP may signal the other detectors that they should prepare to read out.

After sending a L0 signal to the CTP, the detector may send a L1 signal. A L1 signal contains information about the event, and is sent if the internal routines of the detector deems the event to be above sett thresholds. Some detector will only issue a L1 signal as they are to slow or far away from the interaction point. Upon receiving a L1 signal, the CTP will evaluate the information it has received from the signal, the state of congestion of the DAQ/HLT, and the eventual overlap of events. The CTP then makes a decision as to accept or reject the event.

A L2(level 2) signal is emitted by the CTP after it has made a decision. There are two different L2 signals: accept (L2a) reject (L2r). If a detector receives an L2 accept signal, then it will read out. If it receives a L2 reject signal, the corresponding buffer is discarded.

This system protects the TPC, a slow detector due to the 88 μs drift time, from reading out overlapping high multiplicity events, and provides a selective buffer between the high rate of events and the relative low bandwidth/capacity of the DAQ and the HLT.

2.3.4 HLT - High Level Trigger

After a L2a signal has been emitted, the relevant detectors read out and the data is sent to the High Level Trigger (HLT). The HLT is responsible for reducing the huge data rate from ALICE, up to 25 GB/s, to the required data rate of 1.2 GB/s, and to do pre–offline–analysis before committing the data to tape. It is implemented as software on a PC farm.

2.3.5 DAQ - Data Acquisition

The DAQ system is responsible for the data–flow from the detector up to the data storage. It includes the data–flow from the detector electronics up to the DAQ computing fabric and to the High-Level Trigger (HLT) farm, the transfer of information from the HLT to the DAQ fabric, and the data archiving in the CERN computing centre[12].

Chapter 3

PHOton Spectrometer

The PHOton Spectrometer (PHOS) is an high-resolution electromagnetic calorimeter covering a limited acceptance at central rapidity. The main physics objectives are to study jet quenching through measurements of high–p_T π^0, γ–jet correlations and to search for thermal photons from the QGP.

The high particle multiplicity in LHC nuclear collisions require a dense highly segmented calorimeter at a large distance from the interaction point and a detecting material with small Moliére radius and High–energy resolution. The combination of segmentation and distance results in good resolution but increases the cost per unit of acceptance. Dense material and a small Moliére radius decreases the required depth and cell occupancy. High–energy resolution and small Moliére radius is provided by using a dense scintillator material, lead tungstate ($PbWO_4$), at a depth of 20 X_0 it is only 18 cm deep[13].

3.1 Design

PHOS, shown in figure 3.1, has a high granularity with 17 280 detecting channels. Each channel consists of a lead-tungstate crystal, $PbWO_4$ (PWO), $2.2 \times 2.2 \times 18$ cm^3 in size, coupled to a large-area Avalanche Photo Diode (APD)[13].

PHOS is subdivided into five independent modules positioned in a cradle at a distance of 4.6 m from the interaction point. However, during the first run, only 3 modules will be installed. Each module consist of 64×56 PWO crystals arranged in a matrix. PHOS covers approximately a quarter of an unit in pseudo–rapidity, $-0.12 \leq \eta \leq 0.12$, and 100^0 in ϕ angle[13]. A summary of details are given in Table 3.1.

Future plans for PHOS may include the development and installation of a Charged Particle Veto (CPV), a Multi–Wire Proportional Chamber (MWPC), to detect charged particles with an efficiency better than 99%. In this case, the CPV will be constructed as 5 modules. These CPV modules

will then be installed on the PHOS Modules.

Coverage in pseudo–rapidity	$-0.12 \leq \eta \leq 0.12$
Coverage in ϕ angle	$220^0 < \phi < 320^0$
Distance to interaction point	4600 mm
Modularity	Five modules of 3584 PWO crystals
EMC	
Material	Lead–Tungstate (PWO) crystals
Crystal dimensions	$22 \times 22 \times 180$ mm^3 per crystal
Depth in radiation length	20 X_0
Number of crystal	17920, 3584 per module
Total area	8 m^2
Total crystal weight	12.5 t
Operating temperature	-25 C^0

Table 3.1: Properties of PHOS. taken from[13].

3.1.1 PWO Scintillator crystals

The lead tungstate ($PbWO_4$) crystals is selected for PHOS's scintillators due to their physical properties. For details see table 3.2. It was the only material filling the requirements concerning Moliére radius, light yield, and cost[14].

The crystals will be cooled to a temperature of -25^0 C. This increases the light yield by a factor of 2.5 and reduces the electronic noise. Both effects lead to improved energy resolution. The crystals provides an intrinsic timing resolution of ~ 0.13 ns[14, 15].

The assembly of a cell can be seen in figure 3.2.

Density	8.28 g/cm^3
Radiation length	0.89 cm
Molière radius	2.0 cm
Refractive index along z axis ($\lambda = 632$ nm)	2.16

Table 3.2: Properties of $PbWO_4$ crystals. Taken from [14].

3.1.2 APD - Avalanche Photo Diode

The Avalanche Photo Diode (APD) technology was selected for PHOS as its photo–detector. By applying an high reverse bias voltage, APDs show an internal current gain due to impact ionization. Impact ionization is the excitation of an electron to the valence band from the conducting band as

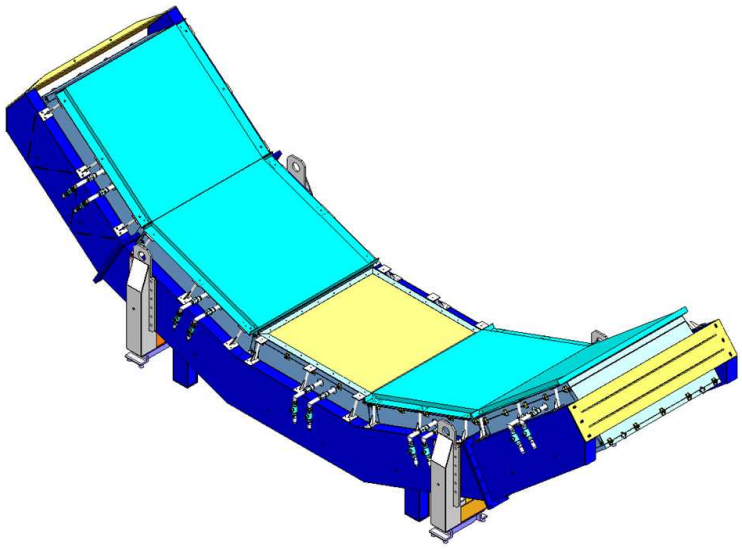

Figure 3.1: Diagram of PHOS. Taken from [13]

a result of a collision by another high energy electron in the conducting band. Furthermore the high voltage of the APD causes such valence band electrons to gain energy, and potentially excite further electrons from the valence band. Thus, a photon striking the APD and exiting an electron to the conducting band will cause an avalanche of electrons, which leads to high current gain. The quantum efficiency of the PHOS APDs is around 85%. [15].

3.1.3 FEE - Front End Electronics

The read-out electronics of PHOS is based on the ALTRO chip, originally developed for the ALICE TPC (ALTRO = ALice Tpc Read Out). The electronic chain includes energy digitization, timing for Time Of Flight (TOF) discrimination, and trigger logic for generating L0 and L1 triggers.

To cover the large dynamic range of photon energy from 100 MeV up to 100 GeV, each energy shaper channel supplies two outputs with low and high amplification digitized in separate ADCs. The gains of the APDs are equalized by means of a control system where the bias is set individually for each APD. The preamplifier is integrated with the APD and mounted on the crystal in the cold volume (-25 C^0). The ALTRO chips and the surrounding control electronics are mounted on cards placed in the warm volume of the PHOS module[9].

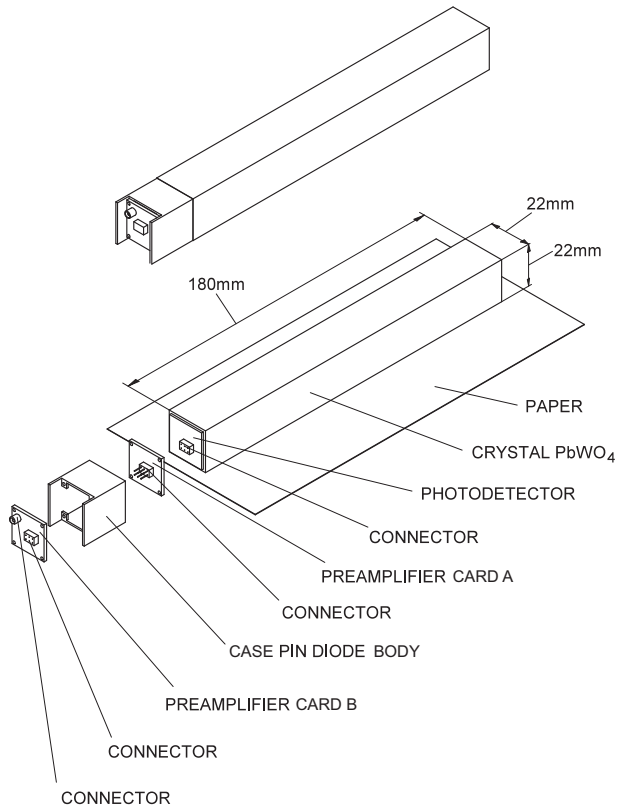

Figure 3.2: A diagram and image of the assambly of a single PHOS cell. The crystal is $PbWO_2$. Taken from [16] and [13].

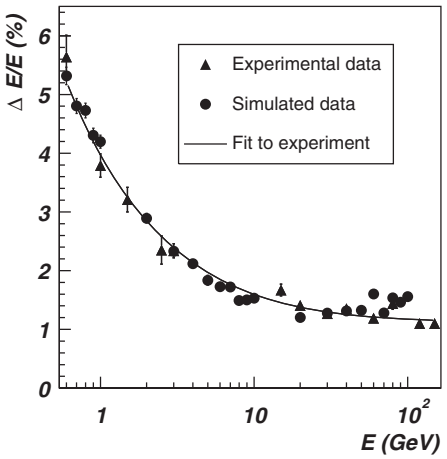

Figure 3.3: Energy resolution of a 3×3 $PbWO_4$ array measured in response to mono–energetic electrons (▲) or calculated with simulations of mono–energetic photons (•). The continuous line represents the result of the fit of equation 3.2 to the experimental data. Taken from[9].

3.2 Energy Resolution

Invariant mass resolution is given by the following expression, which can be deduced from equation 1.12 using a Taylor's expansion for the moments of function uncertainties:

$$\frac{\sigma_M}{M} = \frac{1}{2}\sqrt{\frac{\sigma_{E_1}^2}{E_1^2} + \frac{\sigma_{E_2}^2}{E_2^2} + \frac{\sigma_\Psi^2}{tan^2(\Psi/2)}} \tag{3.1}$$

where E_1 and E_2 are the photon energies(in GeV) and Ψ is the opening angle between the photons. The error of Ψ is determined by the spatial resolution.

The energy resolution can be parametrized as (E in GeV):

$$\frac{\sigma_E}{E} = \sqrt{\frac{a^2}{E} + \frac{b^2}{E^2} + c^2} \tag{3.2}$$

where a is the stochastic term, b is determined by the readout noise, and the constant term, c, is due to detector and readout inhomogeneity and to the calibration error. These terms have been determined empirically[9]. They were obtained by fitting equation 3.2 to the resolution of the measured energy collected in an 3×3 array of EMC crystals upon the impact of mono-energetic electrons and of the calculated energy from simulations of mono-energetic photons performed in identical conditions. See figure 3.3.

3.3 Position Resolution

Position resolution can be parametrized as (E in GeV):

$$\sigma_{x,z} = \sqrt{A_{x,z}^2 + \frac{B_{x,z}^2}{E}} \tag{3.3}$$

The impact position on PHOS is reconstructed by calculating the position of the centre of gravity of the reconstructed cluster. This position is further corrected for by an algorithm which takes incident angle into account. The test beam measurements were extended to verify the incidence on the position resolution by tilting the array of EMC cells by $\alpha = 0$, 3, 6 and 9. Function 3.3 was fitted to the experimentally measured position-resolution of electrons. Results are shown in table 3.3, figure 3.4. They show that position resolution strongly depends on incidence angle [9].

α(degree)	A_x (cm)	B_x $(cm\ GeV^{1/2})$
0^0	0.032	0.264
3^0	0.070	0.231
6^0	0.147	0.170
9^0	0.198	0.155
all angles	0.070	0.229

Table 3.3: Parimeters of PHOS position resolution, taken from[9].

3.4 $\pi^0 \to \gamma\gamma$ acceptance

A study of the PHOS acceptance has been performed by G. Consea et al. and published as a CERN internal note[17]. They define the acceptance of the $\pi^0 \to \gamma\gamma$ in PHOS as the probability that both decay photons hit the active area of PHOS when the π^0 is emitted from the IP within the rapidity interval $|y| < 0.5$ and azimuthal angle $0 < \phi < 2\pi$.

Based on simulations, they found the acceptance to reach a plateau around $\sim 6 - 7\%$ for p_T above $\sim 30GeV$, as can be seen in figure 3.5. This acceptance is low for small p_T due to the wide opening angle of photons, and reach a saturation for high p_T when the opening angle becomes narrow.

The solid lines in figure 3.5 are fits. They are parametric functions representing the dependency of acceptance on p_T and y:

$$f(p_T) = (c_0 + c_1 p_T) e^{\left(-\frac{p_T - c_2}{c_3}\right)} \tag{3.4}$$

$$g(y) = d_0 - d_1 y^4 \tag{3.5}$$

Parameters are found in table 3.4 and 3.5.

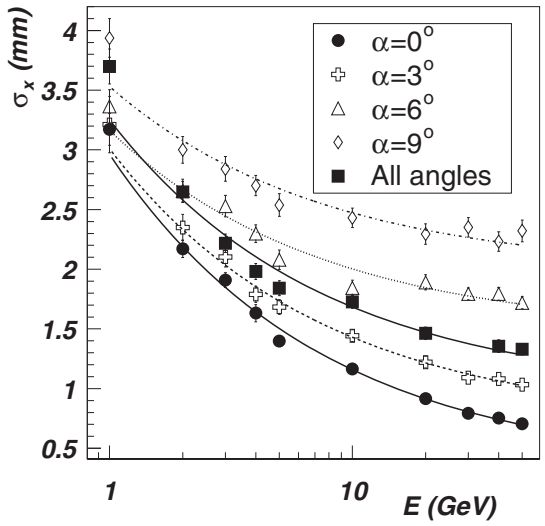

Figure 3.4: Position resolution of PHOS versus the photon energy for the incidence angles on module $\alpha = 0, 3, 6, and\, 9\,^\circ$ and the average for all possible incidences in the ALICE layout. Taken from[9].

Acc. vs. p_T	c_0	c_1	c_2	c_3
$\pi^0(p_T < 10\ GeV/c)$	$0.42(2) \times 10^{-1}$	$0.13(3) \times 10^{-2}$	$0.55(7) \times 10^{0}$	$0.125(16) \times 10^{1}$
$\pi^0(p_T < 100\ GeV/c)$	$0.64(2) \times 10^{-1}$	$0.12(27) \times 10^{-4}$	$-0.14(6) \times 10^{2}$	$0.12(4) \times 10^{2}$

Table 3.4: Parameters of the function 3.4, $f(p_T)$. Taken from [17].

As PHOS will initially run with a maximum of 3 modules, the $\pi^0 \rightarrow \gamma\gamma$ acceptance was also studied with 1, 2 and 3 modules. It was found that the acceptance approximately scales with the number of modules for high p_T. For low p_T, beginning at $\sim 3\ GeV$, the acceptance drops slightly compared to the scaled acceptance, dropping to about half at $\sim 1\ GeV$. It was also found that the acceptance is higher if the modules are positioned adjacently, without gaps. For more details concerning the acceptance of PHOS, especially π^0 and η two photon decay channel, see [17].

3.5 Front End Electronics Card Testing

During week 9 in year 2008 the Front end Electronics Cards (FEC) of the first PHOS module were tested. The test system consisted of an "usb to FEC" (U2F) electronics card and an interactive computer program. The U2F card provides the computer with a interface in which the computer program may use to test the FEC cards. The U2F card was connect to each FEC card via two flat cables, and the computer to the U2F via a usb cable. For each FEC card following test were conducted:

Acc. vs. y	d_0	d_1
$\pi^0(p_T < 10\ GeV/c)$	0.1801 ± 0.0011	393.0 ± 13.0
$\pi^0(p_T < 100\ GeV/c)$	0.2324 ± 0.0013	57.0 ± 17.0

Table 3.5: Parameters of the function 3.5, $g(y)$. Taken from [17].

- BC registers test. This test writes and reads from a set of registers, and compares the output to the written values. If the output does not equal the input, then register is deemed malfunctioning.

- ALTRO registers test. It follows the same procedure as the above test, using a set of ALTRO registers in place of BC registers.

- PMEM test. This test writes a predefined stream of bits to it and reading out. It then compares the in–stream to the out–stream.

- Digital path test. The test is similar to the test above, but reads out the digital output files, as apposed to the pedestal memory stream, and compares the files to the expected result.

here BC stands for Board Control, ALTRO of ALTRO chip(s), and PMEM for pedestal memory.

BC and ALTRO registers are registers that is used by the detector control electronics to give behavioral commands to the FEC chips and receive states and sensor output. This includes information such as temperature and bias voltage. PMEM is the memory that contains the detector APD output while the electronics waits for a read out command from the CTP.

Errors in the ALTRO registers are separated into relevant and irrelevant errors. Since the PHOS FEC design is a based on the TPC FEC design, the TPC test system tests for errors in registers which are not used by PHOS. The cards that show errors in these registries are not considered to be malfunctioning. In addition, several cards did not respond to input. These are counted under “not testable” in the table bellow. The result from the testing can be found in table 3.6.

	112	Cards
No errors found	96	
Errors in ALTRO registers, relevant	1	
Errors in ALTRO PMEM	1	
Not testable	2	
Missing or undergoing maintenance	5	

Table 3.6: Results from FEC U2F testing.

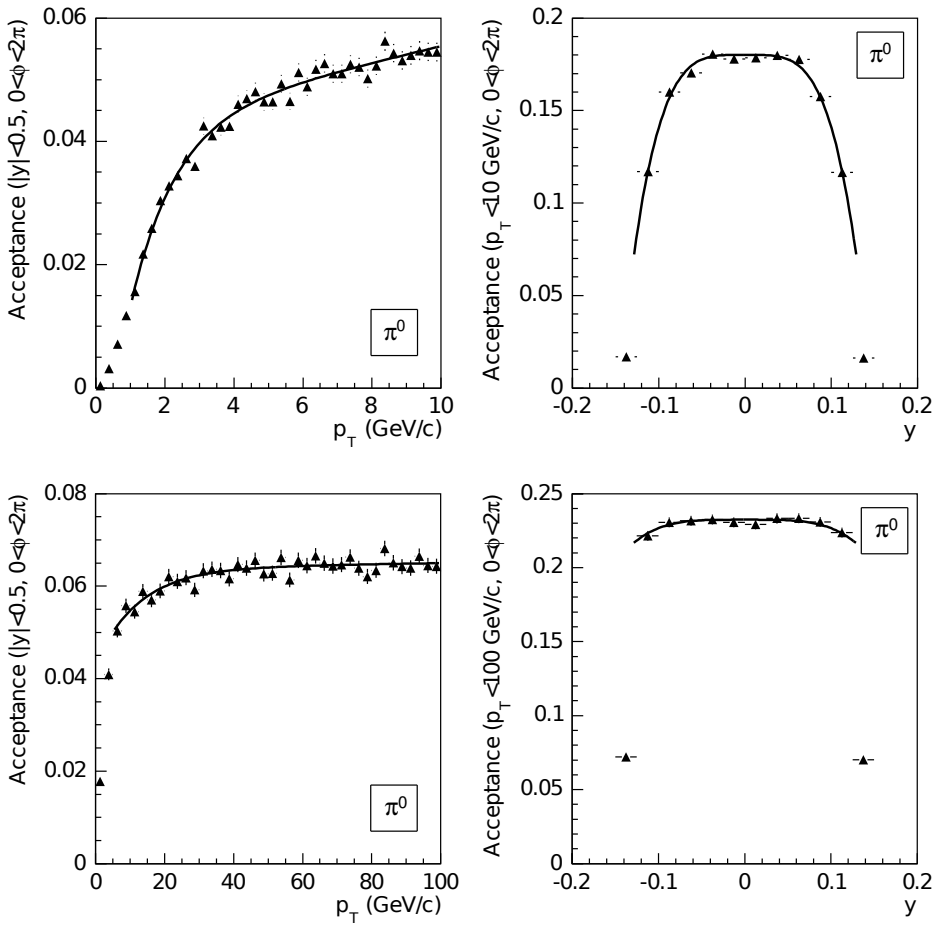

Figure 3.5: Acceptance of PHOS as a function of p_T (left) and y (right) for $0 < p_T < 10\ GeV/c$ (top) and $0 < p_T < 100\ GeV/c$ (bottom), $0 < \Phi < 2\pi$ and $-0.5 < y < 0.5$. taken from[17]

3.6 Cluster Reconstruction

Consider an event, where we have a number of particles that hit and deposit energy in PHOS. This is illustrated in figure 3.6. If PHOS is triggered, then the channels will be read out, and a set of digits D are produced:

$$D \in \mathbb{R}^{17920} \tag{3.6}$$

The cluster reconstruction process should reduce these digits into a set of energies and positions, such that a single particle (j) has a corresponding measured energy E_j and position $\vec{x}_j$.

These digits are converted to cell energies 'ε' via a set of calibration

coefficients 'C' which will be introduced in detail in section 4.2, such that:

$$\varepsilon,\ C\ \epsilon\ \mathbb{R}^{17920} \tag{3.7}$$

$$\varepsilon = C \circ D \tag{3.8}$$

The clustering algorithm then groups the cell energies together into a set of clusters, and overlapping cluster are *de–folded* from each other by the de–folding algorithm. Thus, each cluster Θ_j is a set of cell amplitudes fractions. This can be written as

$$x = \varepsilon \circ f_j \tag{3.9}$$

where f_j is a set of fractions produced by the clustering algorithm and the de–folding algorithm, and the operator '$\circ$' is operator of the Hadamard product[1]. More specifically, f_j is an estimate of the fractions of the total cell energies ε which are from the cluster Θ_j. Another way of writing the above equation, which might better help explain the function of f_j is:

$$f_{jk} = \frac{\Theta_{jk}}{\varepsilon_k} = \begin{cases} 0 & \text{, if } \Theta_j \text{ does not contribute to } \varepsilon_k; \\ 1 & \text{, if } \Theta_j \text{ is the sole contributor to } \varepsilon_k; \\ x : x\epsilon(0,1) & \text{, if } \Theta_j \text{ contributes partly to } \varepsilon_k. \end{cases} \tag{3.10}$$

where f_{jk}, Θ_{jk}, and ε_k correspons to the cell number 'k' of f_j, Θ_j, and ε. Furthermore, f_j is chosen such that the cell energies are simply the sum of all the clusters:

$$\varepsilon = \sum_j \Theta_j \tag{3.11}$$

We may now define the cluster energy E_j such that it is the sum of the cluster cell energies applied to a non–linearity correction. This correction is introduced in section 4.3. It is a second degree polynomial whose coefficients[2] are determined empirically, where

$$E_j = P^{(2)}(E'_j) = n_2 \cdot {E'_j}^2 + n_1 \cdot E'_j + n_0 \tag{3.12}$$

and E'_j is the sum of the elements Θ_{jk} of the cluster Θ_j:

$$E'_j = \sum_k \Theta_{jk} \tag{3.13}$$

In addition, we may now define a cluster position such that it is the weighted center–of–gravity of the geometric positions of the cells where the

[1] The Hadamard product, often called the entery-wise product, results in a matrix where the intries are equal to the product of the corresponding entries of the two input matrixs'. For definition see [18].

[2] see table 4.1, page 37.

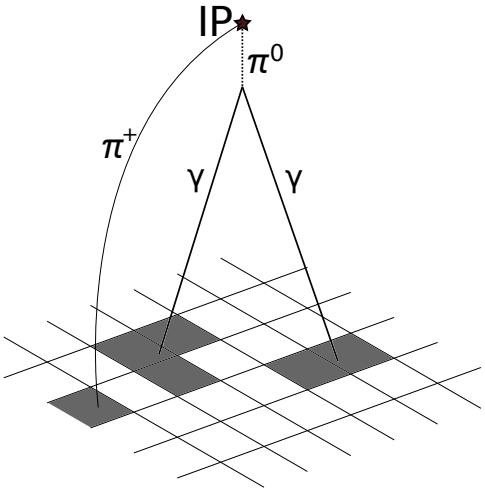

Figure 3.6: Diagram of the surface of PHOS being hit by a set of particles. These particles deposit energy, which is depicted as coloured squares. The squares are portray the upper(non–APD) end of the crystals, and represent cells. The diagram is not to scale.

weights are the cluster energies:

$$\vec{x}_j = \frac{\sum_k \vec{r}_k \Theta_{jk}}{\sum_k \Theta_{jk}} \tag{3.14}$$

where $\vec{r}_k$ and Θ_{jk} is the the position and cell energy of of cell k. The above equation is a simplification, the unsimplified equation can be found in [17].

3.6.1 Clustering Algorithm

For a given event and set of digits, the clustering algorithm select neighboring digits and produces a set of clusters where a cluster is a set of digits. Two digits are neighbours if they are from cells that have a common edge or a common corner[17].

The algorithm starts by considering every digit above a threshold as a seed digit for a cluster. Then, for each seed digit, it applies the following algorithm to produce a cluster:

- Take seed digit and apply it to *step '1.'*

  1 The *digit* is considered part of the cluster and apply it to *step '2.'*

  2 For all neighbours of the *digit* in not yet evaluated;

2.1 if the digit is above a threshold, pedestal noise, then apply it to *step '1'*,

2.2 else, reject the *digit*.

Then, in the likely case of duplicated clusters, all but a single duplicate is discarded. Finally, if the cluster has multiple maxima, where a maxima is a digit where the digit's energy differ from neighbouring digits' energy by more then $30MeV$, then the cluster is de-folded into separate clusters by the de-folding algorithm described in [16].

3.6.2 Shape Analysis

At reconstruction, a set of parameters are calculated that characterise the shape of the clusters. These are

- digit multiplicity: the number of digits in the cluster,
- latter of dispersion: the RMS of weighted cell positions relative to cluster center,
- sphericity parameter/eccentricity: a measure of how the much the shape deviates from being circle shaped,
- core energy: sum of digits within a radius, 3 cm,
- time: shortest timing among digits compared to event generation time.

These parameters are used to calculate the PID values of cluster. A cluster's PID values are a set of estimated probabilities that the cluster originates from a corresponding set of particles [17].

Chapter 4

Calibration Methods

PHOS has 17280 channels. The channels measure deposited energy in the corresponding cell under the assumption that the deposited energy is proportional to the light intensity measured by the APD. In the electronics, the electric feedback from a channel is amplified, digitized, and ultimately reduced to a double precision floating point value called *cell amplitude*. This cell amplitude is then converted into *cell energy*. After this, the cell energies are converted into cluster energies as detailed in section 3.6.

We need to calibrate the parameters of these conversions in order to ensure that the reconstructed cluster energies are as close to the energies of the originating particles as possible. We need to take into account not only the inherent non–linearity of the detector but also variations in sensitivity in–between cells.

On the hardware side, we correct for these variations using individual cell APD bias voltage settings. On the software side, we use the calibration coefficients. A cell's amplitude is converted to energy by taking *cell energy* to be the product of the *cell amplitude* and the *calibration coefficient* (CC), where each cell has a unique CC. Last, the clusters are reconstructed, and a non–linear correction is applied.

4.1 APD Bias Voltage and Gain

The APD bias voltage is the voltage applied to the APD photo diodes, and it dictates the response of the APDs to scintillation light. The PHOS FEE is designed so that the APD bias voltage can be individually set for the channels with a resolution of $0.2\frac{V}{bit}$ and a stability of 0.1%[19]. This is used to equalize the gain of the energy channels using the method in section 4.4.

The gain of a channel is the degree the APD and corresponding electronics increases the signal caused by scintillation light on the APD. Equalization of gains is the state in which all channels produce an equally large signal in response to equal amounts of deposited energy in the crystals.

4.2 CC - Calibration Coefficient

As explained in the beginning of this chapter, a set of *'Calibration Coefficients* (CCs) are used by the software to convert cell amplitudes to cell energies by taking a cell energy to be the product of the cell amplitude and the corresponding CC. The CCs are implemented as double precision float numbers. Compared to the APD bias voltage settings they are virtually continuous. Also, they have the advantage of being applicable after the data run as apposed to the APD bias voltage settings which must be applied before the data run.

4.3 Non–Linear Effects and -Correction

A non–linear detector is a detector that does not respond to input in a way such that the output is a linear function of the input. A non–linear effect is a property of the detector/setup that causes the detector to become non–linear.

APDs produce their output via a avalanche of exited electrons/electron holes. As these avalanches become large and numerous, the APD's valence layer becomes increasingly saturated with electrons and the probability that a accelerated electron/hole further excites electrons is reduced. This saturation is a non–linear effect.

An EM shower (see section 1.5.7) in PHOS will typically deposit its energy in several crystals. It might be that one or more of these crystals does not attain the amount of energy needed to rise above the statistical noise, and it will therefore not pass the zero–suppression cut statistically. When the cluster is reconstructed, the energy of the cluster is to first approximation equal to the sum of the cell energies. If one or more cells are not read out, due to them not passing the zero–suppression cut, then the cell is not included in the cluster reconstruction. The sum of cell energies method used in PHOS does therefore not account for the full particle energy. This is another non–linear effect called *horizontal leakage*.

After a couple of radiation lengths, an EM shower deposits its energy according to equation 1.16 where 'z' is the depth in the crystal. PHOS measures energy by measuring the light intensity. Intensity is proportional to the energy emitted by the source. In the case of PHOS case, it is equal to the deposited energy. However, it is also a function of the distance between the source and the point of intensity, given by equation 4.1,

$$I = \frac{P}{4\pi r^2} \tag{4.1}$$

where P is the energy radiated per second, and r is the distance from source to point. This effect is partly countered by the reflective coating around the crystals. However, it is still a major non–linear effect.

While most of the electro-magnetic shower started by photons is inside the PWO crystal, some energy may leak from the back of the crystal when the incident energy of the photon is large[20]. This is a non–linear effect.

These non–linear effects are corrected for by a second degree polynomial where the coefficients are determined empirically using either real data or simulated data. The correction is applied to the total cluster energy, not the cell energies[21]. These parameters can be found in table 4.1.

n_0	=	2.41×10^{-2}
n_1	=	1.05×10^{0}
n_1	=	2.49×10^{-4}

Table 4.1: Parameters of the non–linear correction, function 3.12 page 32, in AliRoot version v4-16-Release.

4.4 Equalisation of Gains Using Total Measured Energy

One method for equalisation of gains is to scale the gain using the sum of deposited energy, cell by cell, over a large number of events. At LHC collision events(p–p and Pb–Pb), the distribution of particles and particle energy is approximately isotropic over the limited pseudorapidity covered by PHOS ($|\eta| < 0.12$). However, due to the geometry of PHOS the distance from the IP increases from the center of the module to the edge by about ~ 2 %. If we assume a isotropic distribution, then the edge cells should only experience a decrees in particle intensity relative to the center cell of ~ 4 %. If we apply a 200 MeV cut on the cluster energy, then the amount of secondary particles(particles not from the IP) becomes negligible with respect to total accumulated cell energy[20].

As the cells are approximately equally radiated, the sum of irradiation in a cell over a large number of events should be equal to that of the other cells. Equalization is then achieved by taking the average sum and scaling all channels such that their gain becomes equal to that of the average.

This technique can be used to parametrize both the APD bias voltage settings and the CCs, but mostly it will be used to calibrate the bias voltage settings as there are better techniques for calibrating CCs. It is expected that this technique should yield a relative energy calibration of 7%[20].

4.5 Calibration using MIP from cosmic rays

At ground level, 98% of charged cosmic particles are $\mu^{\pm}$. The momentum of these particles are distributed with a wide peak between ~ 10 and $\sim 100\ GeV$ for vertical cosmic muons. In the probable momentum range of these cosmic muons, energy loss occurs mainly through collisions as described by the Bethe–Bloch equation. (see section 1.5.1). According to Bethe–Bloch, the muon has a minimum energy loss per distance ($\frac{dE}{dx}$) at $p \simeq 0.3\ GeV$ in PWO crystals. Therefore, the cosmic muons are approximately Minimum Ionizing Particles (see section 1.5.2), and deposit approximately $\Delta E \simeq 0.2\ GeV$ when traversing PHOS.

The measurement of deposited energy from cosmic muons passing through a single crystal is directly comparable to the result expected from the Bethe–Bloch. Using a cell MIP peak, based on several measurements, the gain can be scaled such that the peak coincides with that of the other channels and the expected result. As the cosmic muons have a wide distribution, the MIP peak will also be wide. This will negatively effect the amount of statistics needed to accurately estimate the peak position. Cosmic muons will therefore not be used for the final calibration[20].

4.6 Calibration using MIP from collisions

In nuclear collisions at LHC, the produced particles consist of various hadrons and leptons. Charged pions ($\pi^{\pm}$) are one of the most abundant type of particles along with π^0. A cluster energy distribution from a relatively small number of nuclear collisions will contain a MIP peak from $\pi^{\pm}$ penetration.

While a collision $\pi^{\pm}$ peak will be wide, large amounts of statistics can quickly be generated. This large amount of statistics makes a collision based MIP peak a better calibration tool then that of a cosmic MIP peak, and it may be used to calibrate the CCs. It is expected that this technique should yield a relative energy calibration of 2.4%[20].

4.7 π^0 Invariant–Mass peak

A proton–proton collision produces on average ≈ 4.4 neutral pions per unit rapidity at mid rapidity according to PYTHIA. A π^0 will almost immediately decay to two photons: $\pi^0 \rightarrow \gamma\gamma$. If these two photons are detected by PHOS, then the π^0 invariant mass (IM) can be reconstructed, and the reconstructed mass peak can be compared to the ideal π^0 mass (m_{π^0}). As we will show in section 4.8.3, the peak scales with the cluster energy, and cluster energy with cell energy.

However, we need to know the momentum and energy of the photons in order to reconstruct a π^0 IM. As a photon has no mass, the magnitude of its

momentum is given by and is equal to its energy divided by the speed of light. The direction of its momentum can be estimated using the approximation that the photon originate in the IP. This approximation is valid due to the short life time of the π^0. It has a mean path length before decay of $\simeq 25\beta\gamma\ nm$ which is small compared to the distance between the IP and PHOS 4.6 $m = 4.6 \times 10^9 nm$. Thus, the direction is given by the vector spanned by the IP point, and the position of the cluster measured points in PHOS.

Another requirement of a IM reconstruction is that both photons hit the detector. Details on the π^0 acceptance of PHOS can be fund in section 3.4. The amount of π^0 per event effects the amount of eventes needed to perform calibration.

Another issue that must be addressed is that a single π^0 IM reconstruction is not the result of a measurement in a single channel. A IM is calculated on the basis of two clusters. Each cluster is calculated on the basis of several channels. As all the channels are biased in a decalibrated model, the IM will be shifted in a very intricate way, and it is not obvious how the IM can be used to correct the bias of any single channel.

4.7.1 Invariant Mass Reconstruction

Consider an event. We have a number of particles hitting and depositing energy. Consider that we have used the technique presented in section 3.6 to reconstruct the digits into clusters, with corresponding cluster energies (E_j) and cluster positions ($\vec{x}_j$).

Consider the case where we pick two clusters. We can use the right hand side of equation 1.11 to reconstruct the *invariant mass* (M) of sum of the two particles. If the two particles originate from a π^0, then the invariant mass of the pair should be the same as the mass of the π^0, i.e. $m_{\pi^0} = 134.9\ MeV$

However, equation 1.11 requires not only the energies of the particles but also the momenta. Assuming they are photons, then the magnitudes of the momenta is equal to the energy:

$$|\vec{p}_j| = E_j/c \tag{4.2}$$

If the particles are photons then they will fly in a straight path. If they originate from the IP and hit PHOS, then the directions of the momenta can be calculated using the positions measured in PHOS

$$\frac{\vec{p}_j}{|\vec{p}_j|} = \frac{\vec{x}_j - I\vec{P}}{|\vec{x}_j - I\vec{P}|} \tag{4.3}$$

$$\vec{p}_j = \frac{\vec{x}_j - I\vec{P}}{|\vec{x}_j - I\vec{P}|} E_j/c \tag{4.4}$$

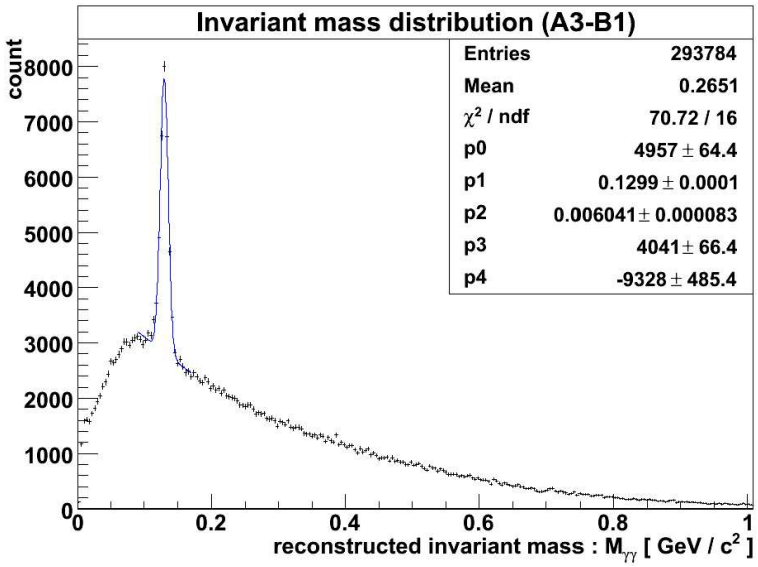

Figure 4.1: π^0 invariant mass plot. The reconstructed invariant masses of all combinations of clusters above a π^0 $p_T > 1Ge/cV$ and $e < 0.8$. Based on 4×10^6 p–p events. Taken from [20].

4.7.2 Event Number Requirements

Fumihiro Chuman et al.[20] did a study on π^0 recalibration. They simulated 4×10^6 14 TeV p–p events with only PHOS in the ALICE geometry using PYTHIA and GEANT3. They produced an invariant mass plot using a $p_T > 1GeV$ and $e < 0.8$[1] cut on π^0 transverse momentum and found the IM peak to contain $60'801 \pm 824$ entries, shown in figure 4.1. This indicates that a p–p event produces at average 0.0152 ± 0.0002 reconstructable π^0 photons pairs in PHOS using the cuts described above.

PHOS has $5 \times 64 \times 56 = 17'920$ cells, assuming 5 modules. Therefore, the amount of p–p events needed to produce at average 1 π^0 IM entry per cell assuming the above ratio is:

$$N_{events} = \frac{N_{cells}}{N_{\pi^0}/N_{events}} = \frac{17'920}{0.0152} = 1.789 \pm 0.016 \times 10^6 \qquad (4.5)$$

It is more realistic to assume that the technique needs around 100 events per channel. In this case, we need $\sim 1.8 \times 10^8$ p–p events to apply the technique.

4.8 π^0 Invariant Mass Plot

A π^0 invariant mass plot is a plot where a set of results from invariant mass reconstructions is filled into a histogram. The π^0 peak of such a plot can be

[1] The parameter 'e' is described in section 4.8.2, page 42

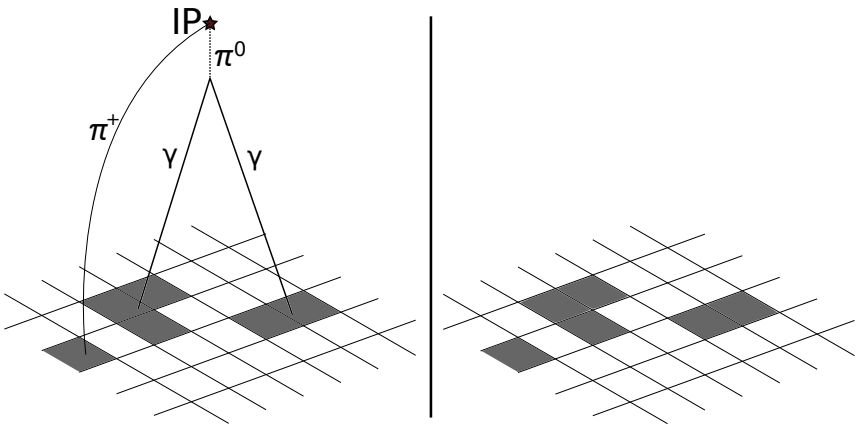

Figure 4.2: Combinatorial Background. On the left we see a depiction of particles hitting PHOS cells. On the right we only see the clusters where they deposited energy. When analyzing PHOS data, we only have information about the deposited energy, as depicted on the right.

used as a measure of the resolution of the detector, as seen in function 3.1 and discussed in section 5.1. It can also be used to correct for the calibration of a single cell, and we attempt to argue for this in section 4.9.

But first we discuss a major issue concerning these plots, combinatorial background, and how to deal with this issue.

4.8.1 Combinatorial Background

We do not know which pairs of clusters in PHOS stem from a $\pi^0 \rightarrow \gamma\gamma$ source. This is depicted in figure 4.2. We are therefore forced to make educated guesses based on the shape and energy of the clusters and the output of the inner tracking detectors. Inevitably, a fraction of the reconstructed masses in a IM plot are not from such a decay. This fraction contributes to the background of the IM plot. We call this source of background for combinatorial background.

This will most likely effect plots basedon Pb–Pb more severally than those based on p–p due to the multiplicity. The multiplicity (M) may be up to $2-3$ orders of magnitude higher central Pb–Pb events compared to p–p. The amount of π^0s in a single event scales roughly with M. However, the combinatorial background scales roughly with M^2. Thus, the increase in multiplicity when going from p–p to Pb–Pb is both an advantage and a disadvantage.

4.8.2 Cuts

The combinatorial background can be reduced by applying cuts. Here we will discuss some of the possible cuts that can be applied for maximizing the peak to background ration in π^0 invariant mass plots.

Cluster Energy Cut

Using a cluster energy cut, limiting clusters to above 0.5 GeV, will severely reduce the amount of combinatorial background, as there is a large amount of photons below the cut. In addition to low energy photons, minimum ionizing particles deposit a energy of $\sim 0.2\ GeV$. Therefore, the cut will most of the MIP particle clusters.

The impact of the cut on the amount of reconstructed π^0 particles is small. The π^0 acceptance of PHOS drops severely below $\sim 1\ GeV$ momentum.

Even Energy Cut

The photons from a $\pi^0 \rightarrow \gamma\gamma$ decay, are correlated in energy and emission angle. An even energy cut might reduce the background. The evenness of the energy of two photons can be described as:

$$e = \frac{|E_1 - E_2|}{E_1 + E_2} \tag{4.6}$$

A cut of $e < 0.8$ is frequently used.

Photon Probability Cut

The *AliESDCaloCluster* class includes a set of Particle IDentification (PID) values. The photon PID value ranges from zero to one, and is a estimate of the probability of the cluster being that of a photon, see section 3.6.2 A photon probability cut will reduce the combinatorial background caused by non–photon clusters.

The PID is based on time–of–flight information and shower shape analysis. Furthermore, if PHOS is complimented by a Charged Particle Veto (CPV), then CPV–cluster EMC[2]–cluster correlation will also contribute to the cluster PID analysis. PID values will also be used to flag photons that are the result of a $\pi^0 \rightarrow \gamma\gamma$ decay. For more information see [9].

4.8.3 Mathematical Model

Consider a set of events where each has a set of clusters. Using equations 3.12, 3.14, and 4.4. we calculate a set of energies (E_i) and momenta (P_i) of

[2]EMC - crystal part of PHOS

the event *'i'*, assuming that the clusters are from photons:

$$E_i \, \epsilon \, \mathbb{R}^{N_i} \tag{4.7}$$

$$P_i \, \epsilon \, (\mathbb{R}^3)^{N_i} \tag{4.8}$$

where N_i is the number of clusters in event 'i'. These energies and momenta can be described as a sets of four–vectors (p_i) using equation 1.7

$$p_i \, \epsilon \, (\mathbb{R} + \mathbb{R}^3)^{N_i} \tag{4.9}$$

$$(p_{ij})^\mu = (E_{ij}, \, \vec{p}_{ij}) \tag{4.10}$$

where E_{ij} and $\vec{p}_{ij}$ is the energy and momentum of cluster 'j' of event 'i'.

Using these sets, we can combine clusters and use the right hand side of equation 1.11 to produce a invariant mass plot:

$$\begin{aligned} \hat{p}_i = \{(A, B) \; : \; & A, B \leftarrow p_i \\ & A \neq B\} \end{aligned} \tag{4.11}$$

$$\begin{aligned} M_i = \{x \; : \; & x = (A + B)^\mu \cdot (A + B)_\mu; \\ & (A, B) \leftarrow \hat{p}_i\} \end{aligned} \tag{4.12}$$

According to this function, M_i is now a set of invariant masses from event 'i'. The IM plot shows the distrobution of the invariant mass from all events.

4.9 π^0 Cell Invariant Mass plot

As was mentioned in section 4.7, a single π^0 reconstructed IM is calculated on the basis of the response of several channels in two different clusters, and a reconstructed IM is dependent on the calibration of all these channels.

However, it is the central cells of the two clusters that contribute the largest amount of energy to the clusters, and reconstructed IM is strongly dependent on the energy of the clusters, as apparent in equation 1.12. We can use this to construct a IM plot where the π^0 IM peak is strongly dependent on the energy (and thus the CC) of a specific cell/channel.

Consider that we have a set of reconstructed IMs. For a specific cell/channel, take all reconstructed IMs that have a the cell as one of the two clusters' central cell and plot these in a IM plot. We call this type of plot a *cell* π^0 *Invariant Mass plot* and attempt to show that the π^0 peak of this plot approximately scales with the CC of the cell. This is important because a simple scalar relationship between the peak and the CC can be used to calibrate the CCs.

Scalability

A single IM reconstruction is done with equation 1.12. If we take the partial derivative of that equation with respect to the CC of the central cell we get:

$$\frac{\partial}{\partial c_c}M^2 = \frac{\partial}{\partial c_c}2E_\gamma E_{\gamma'}(1-cos(\theta)) = \frac{\partial E_\gamma}{\partial c_c}2E_{\gamma'}(1-cos(\theta)) \tag{4.13}$$

where c_c is the CC of the central cell and E_γ is the energy of that cluster. We make the approximation that $\frac{\partial}{\partial c_c}(1-cos(\theta)) << \frac{\partial E_\gamma}{\partial c_c}$.

$E_{\gamma'}(1-cos(\theta))$ is guarantied to be positive because of the limited geometric acceptance of PHOS $\Delta\Psi < 100^0$ and $|y| < 0.12$. For this argument we are only interested in the sign, so we reduce it to a positive constant 'k'.

$$\frac{\partial E_\gamma}{\partial c_c}2E_{\gamma'}(1-cos(\theta)) = \frac{\partial}{\partial c_c}E_\gamma k \tag{4.14}$$

If we substitute E_γ using equation 3.12 then:

$$k\frac{\partial}{\partial c_c}E_\gamma = k\frac{\partial}{\partial c_c}P^{(2)}(\sum\Theta_\gamma) = k\frac{\partial P^{(2)}}{\partial\sum\Theta_\gamma}\frac{\partial\sum\Theta_\gamma}{\partial c_c} \tag{4.15}$$

where Θ_γ is a set of the cluster energies of cluster γ. The second degree polynomial must be increasing as a function of energy, so we absorb it into the constant:

$$k\frac{\partial P^{(2)}}{\partial\sum\Theta_\gamma}\frac{\partial\sum\Theta_\gamma}{\partial c_c} = k'\frac{\partial}{\partial c_c}\sum\Theta_\gamma \tag{4.16}$$

If we substitute Θ_γ using equation 3.9 and 3.8, then

$$\begin{aligned} k'\frac{\partial}{\partial c_c}\sum\Theta_\gamma &= k'\frac{\partial}{\partial c_c}\sum\varepsilon\circ f_\gamma \\ &= k'\frac{\partial}{\partial c_c}\sum C\circ D\circ f_\gamma \end{aligned} \tag{4.17}$$

where 'C' is a set containing the calibration constants

$$c_c \subset C \tag{4.18}$$

Since 'D' and f_γ are positive constants:

$$\begin{aligned} k'\frac{\partial}{\partial c_c}\sum C\circ D\circ f_\gamma &= k'\frac{\partial}{\partial c_c}c_c d_c f_{\gamma c} \\ &= k' d_c f_{\gamma c} = k'' \end{aligned} \tag{4.19}$$

or

$$\frac{\partial}{\partial c_c}M^2 = k'' \tag{4.20}$$

where k'' is a positive constant and 'M' is a the invariant mass.

This tells us that if we increase the CC then we increase the invariant mass, i.e. the invariant mass scales with the CC of central cell. Because of this, a π^0 invariant mass peak shifts/scales with the central cell CC as the peak is a set of invariant masses.

However, this result also tells us that the peak also scales with the CC of the surrounding cells and the cells of the other clusters. But, if we assume that the CCs are approximately distributed symmetrically around a ideal value, then the effect of these *other cells* should approximately average out.

4.10 Calibration Using π^0 Cell IM Plot

In the previous section we showed that a cell π^0 invariant mass plot approximately scales with the center cell's CC, but also with the biases of the surrounding cells and cells of the other cluster.

We assume that the effects of the biases of the other cells is not large factor compared to that of the center cell. This assumption allows us to make a correction to the center cell CC. We do however recognise that the scaling of the peak is only an approximation valid close to the value of the CC which the cell IM peak is based on.

We have several options when correcting for the CCs. We will use two different options. A scaling equation

$$c_c^{(i+1)} = c_c^{(i)} \times (1 - \frac{m_{peak}^{(i)} - M_{\pi^0}}{M_{\pi^0}}) \tag{4.21}$$

and a slowly converging[22] equation

$$c_c^{(i+1)} = c_c^{(i)} \times (1 + \left(\frac{M_{\pi^0}}{m_{peak}^{(i)}}\right)^2)/2 \tag{4.22}$$

where $c_c^{(i+1)}$ is the new center cell CC, $c_c^{(i)}$ is the old center cell CC, M_{π^0} is the mass of the neutral pion, and $m_p^{(i)}$ is the center of the π^0 cell IM peak.

4.10.1 Algorithm

The major work of plotting a cell π^0 IM peak is:

- Loading the data to memory
- Re–calculating the cluster energies and positions
- Calculate the IM of every cluster pair

We observe that we can create cell π^0 IM peaks for all the cells in parallel by filling the IM of cluster pairs into histograms belonging to the center cells of the clusters.

With the point made in the previous paragraph and equation 4.22, we formulate the following algorithm:

1 Plot the cell IM plots for all the cells using the old CC

2 Find the center of the cell π^0 IM peaks by fitting the plots by a Gaussian distribution

3 Use the peak centers to calculate a new set of CCs using equation 4.22

4 Repeat until calibration is achieved using the new CCs from step 3 in step 1

This technique should provide both relative and absolute calibration of the CC. It also provides calibration using photons which is the particle PHOS is primarily focused on measuring.

Chapter 5

Implementation And Results

In this chapter, we will look at an implementation of the algorithm presented in chapter 4.10, which uses the $\pi^0 \rightarrow \gamma\gamma$ decay channel to calibrate the cells of PHOS. We will also look at the results of the implementation applied to simulated data.

We shall attempt to answer the following questions. Is calibration of PHOS' calibration coefficients (CCs) using π^0 invariant mass reconstruction viable? If so, how large is the amount of statistics needed; and what level of calibration will the technique yield?

5.1 Measures Of Calibration

Before we can evaluate the effectiveness of a calibration algorithm, we must define a measure of calibration. We use the π^0 IM peak width as one such measure of calibration. It is a convenient measure as the calibration algorithm produces a IM plot every iteration. Another measure we will use is the RMS of the CCs.

Peak Width - Standard Deviation

A very accurate calibration would result in a narrow π^0 IM peak centered around the ideal value. In contrast, a uncalibrated detector would have a wider peak. Therefore, a intuitive measure of calibration is the width of the reconstructed π^0 IM peak.

Since we need to decouple the peak from the background, we take the standard deviation of the Gaussian from the following function fitted to the plot. The sum of a Gaussian, for the peak, and a 2. degree polynomial, for the background. This standard deviation is our main measure of calibration, mainly because its applicable to both simulated and real data.

CC RMS

In simulation, the internal structure of every channel is ideal. Therefore, every channel has the same inherent gain, and all the CCs are equal for a perfectly calibrated detector, i.e. ideal calibration.

Consider the root mean square (RMS) of the CCs. This RMS can be represented in percentage. An ideally calibrated model would have a 0% calibration and 10% calibration refers to a state of calibration where the RMS of the CCs is 10%. We will use the RMS of CCs as a measure of calibration.

5.2 Dependency of π^0 peak on energy

As discussed in the previous section, the width of the π^0 peak is a measure of the calibration. However, calibration is not the only parameter that affects the width, it is also affected by the π^0 momentum. This is shown on the top of figure 5.1.

The basis for each point is 5000 single mono–energetic π^0 events simulated using geant3 with AliRoot version v4-15-Release. The π^0 are aimed towards PHOS with the azimuthal angle of $260° < \phi < 280°$ and the angle relative to beam axis equal $80° < \theta < 100°$. μ and σ correspond to the mean and standard deviation of a Gaussian distribution fitted to the reconstructed IM peaks.

We observe from the figure 5.1 that the IM peak width is narrow in the region $\sim 3-30\ GeV$, and that it increases at low and high π^0 momentum. As discussed in section 3.2, the reconstructed π^0 mass resolution is dependent on the cluster energy resolutions and the position resolution, see equation 3.1 page 27.

The width at low momentum can be explained by PHOS's energy resolution. The energy resolution depends on the the photon energy, and this transfers into a dependency on π^0 momentum. When the π^0 momentum decreases, the photon energies decrease, which causes a relative cluster resolution to drop. When the relative cluster resolution decreases, the resolution of reconstructed π^0 masses decreases.

The increasing peak width at high π^0 momentum is probably due to two factors. Firstly, as the $\pi^0 \rightarrow \gamma\gamma$ opening angle becomes increasingly narrow and the relative angle resolution decrease if the position resolution is fixed. Secondly, the increasing probability and degree of overlap of the two clusters as the π^0 momentum increases. In order to reconstruct overlapping clusters, the cluster algorithm estimates the fraction of each clusters contribution to the total cell energy[1]. However, this cause an additional statistical error in the reconstructed energy and position as the algorithm estimates these

[1] As described at the end of section 3.6.1, page 33.

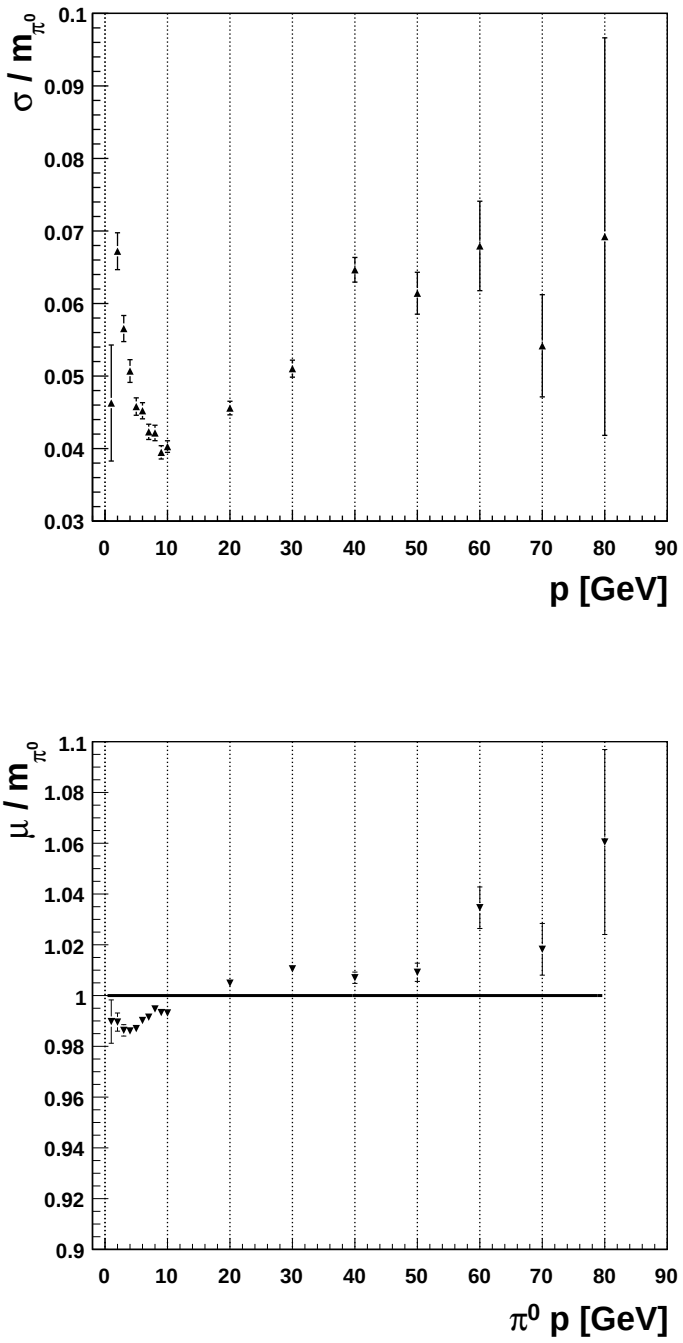

Figure 5.1: The π^0 invariant mass peak width(upper) and position(lower) as a function of π^0 energy. Based on single mono–energetic π^0 events, simulated and reconstructed by use of AliRoot version v4-15-Release.

fractions by the shape of the cluster.

In addition to the reduction in resolution, there is an increase in the uncertainty in the resolution at high and low momentum, and it is due to reduction in statistical entries. At low energies, the probability that both photons from a $\pi^0 \rightarrow \gamma\gamma$ decay hits PHOS decreases as the π^0 momentum decreases, see section 3.4. At high energies, the ability of the shape analysis algorithm to distinguish between a a single high energy photon and two photons from a π^0 decreases as the opening angle decreases. The two clusters merge into one. Simply put, PHOS is only able to reconstruct π^0s with a good probability in the π^0 p_T range of $\sim 1 - 50\ GeV$. These results are in good agreement with those found in [9].

The position of the π^0 invariant mass peak is also dependent on momentum. We observe this in figure 5.1. The position in the high and low π^0 momentum is uncertain, but in the momentum range of $\sim 3 - 30\ GeV$ the peak varies from the expected value with about $\pm 1\%$.

This deviation from expected/ideal value is a clear indication of the level of calibration found in the default reconstruction parameters in AliRoot version v4-15-Release.

Some degree of deviation is inevitable as the non–linearity of the detector is corrected for by a second degree polynomial. In addition, the imperfection in the reconstruction of cluster incident position might also cause deviation in the π^0 peak position.

5.3 Dependency of π^0 peak on calibration

Since we are using two different measures of calibration, it is important to determine the relationship between the two. Using a set of simulated single 10 GeV π^0 events, cluster positions and energy were recalculated with various states of decalibrated CCs. These states are created by randomly distributing the CCs using a Gaussian distribution. For each state, a π^0 reconstructed IM plot is calculated. The result is shown in figure 5.2.

The event set consists of 10000 events containing a single 10 GeV π^0, emitted towards PHOS at an angle of $265° < \phi < 275°$ and $85° < \theta < 95°$, simulated using AliRoot version v4-15-Release.

The CCs where distributed with a Gaussian mean ($\mu_{cc} = 1$) and various standard deviations (σ_{cc}). It was assumed that '1' is the "ideal CC", the value used in reconstruction of simulated data. However, at $\sigma_{cc} = 0$ the peak position is found to be $\mu_{0\%}/m_{\pi^0} = 0.966(1)$. In contrast, the peak position of the IM plot without re–calculating the clusters is found to be $\mu_{\text{no–recalc}}/m_{\pi^0} = 0.993(1)$. The ratio between the two is

$$\frac{\mu_{0\%}}{\mu_{\text{no–recalc}}} = \frac{0.966(1)}{0.993(1)} = 0.973(1) = 1 - 0.027(1) \tag{5.1}$$

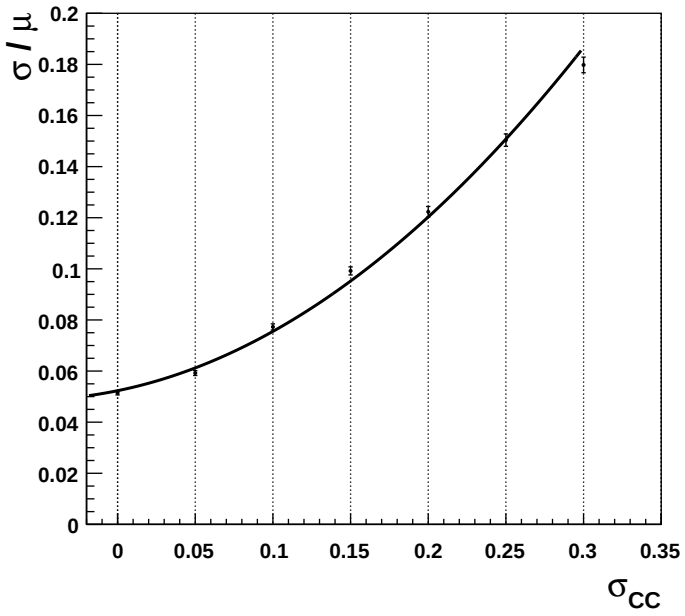

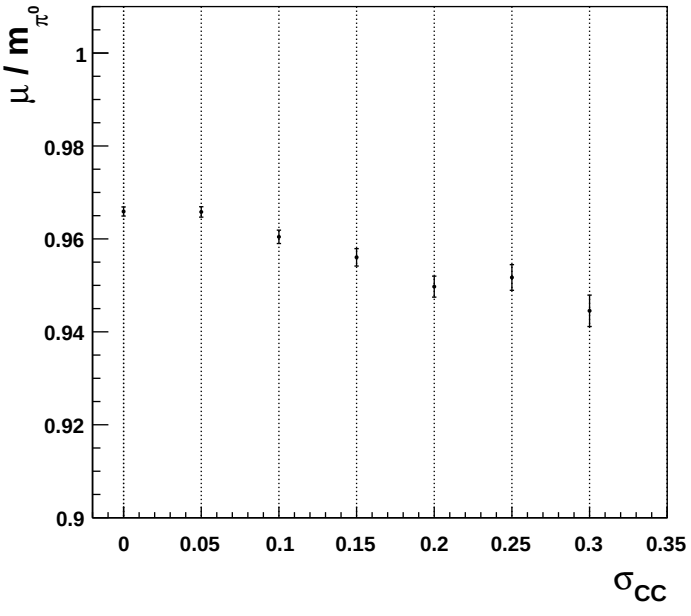

Figure 5.2: The π^0 invariant mass peak width (σ_{π^0}) and position (μ_{π^0}) as a function of CC RMS (σ_{CC}). is the standard deviation of the calibration coefficiants. Based on single mono–energetic π^0 events decalibrated by re–setting the CCs using a gausian distribution, simulated and reconstructed by use of AliRoot version v4-15-Release.

where errors are calculated by the fitting algorithm and propagated using a Taylor's expansion for the moments of function uncertainties.

There is no difference between no–recalculation and 0% recalculation ($\mu_{cc} = 1$, $\sigma_{CC} = 0$) when applying the code to a data set created using AliRoot version v4-15-Release. The change between the two versions is most probably due to a addition of light attenuation consideration that was added in AliRoot v4-16-Release simulation[23].

While the change in peak position is puzzling, it is not a major issue. It implies that the ideal simulation CC is not equal one, but probably slightly higher, $\sim 3.5\%$ higher, using the linear approximation seen in equation 4.20.

One can now ask the question, "How does this shift in peak position when re–calibrating the clusters with $\mu_{cc} = 1$ and $\sigma_{cc} = 0$ effect the peak width?" Using the scaling approximation seen in section 4.9, we would expect that both the width (σ) and position (μ) scales with the same coefficient.

$$\left(\frac{\sigma}{\mu}\right)_{\text{no–recalc}} = \left(\frac{\sigma}{\mu}\right)_{0\%} \tag{5.2}$$

We calculate these ratios

$$\left(\frac{\sigma}{\mu}\right)_{\text{no–recalc}} = 0.0513(8) \tag{5.3}$$

$$\left(\frac{\sigma}{\mu}\right)_{0\%} = 0.0515(8) \tag{5.4}$$

$$\tag{5.5}$$

and observe no significant difference between them.

The solid line seen in figure 5.2 is a fit to the graph of a 2.degree polynomial

$$f(\sigma_{cc}) = \left(\frac{\sigma}{\mu}\right)_{\pi^0}(\sigma_{cc}) = c_2 \cdot {\sigma_{cc}}^2 + c_1 \cdot \sigma_{cc} + c_0 \tag{5.6}$$

where σ_{cc} is interchangeable with RMS_{cc}. Assuming this equation, the peak width at 10% calibration is

$$f(0.1) = 0.0755(8) \tag{5.7}$$

$c_0 = 5.231(51) \times 10^{-2}$
$c_1 = 1.242(54) \times 10^{-1}$
$c_2 = 1.079(32) \times 10^{0}$

Table 5.1: Parameters of function 5.6 fitted to figure 5.2(upper).

5.4 Implementation

The first version of the algorithm has been implemented by B. Polichtchouk. He tested the implementation using 3×10^4 single 10 GeV π^0 events aimed towards PHOS. He found that the implementation calibrated $\sim 1/5$ of a 10% decalibrated module to $\sim 2.7\%$ using σ_{CC} as a measure for calibration[24]. It was implemented in a pair of AliRoot C INTerpretor (CINT) scripts.

Given that the amount of statistics required to calibrate a full PHOS module is above $\sim 1.8 \times 10^8$ p–p events, it is not viable to do full scale calibration as a single process, especially not via an interpreter. The analysis needs to be performed in parallel processes.

AliAnlysis is a framework for parallel event analysis in ALICE. It is intended to be the standard framework for doing large scale analysis on ALICE data and allows the user to write code that will run locally, on the CERN computing center CERN Analysis Facility (CAF) via a system called Parallel ROOT Facility (PROOF), and on the international LHC Computing Grid (LCG) using the middleware ALICE Environment (ALIEN). The algorithm was implemented to take advantage of the parallelism offered by the AliAnalysis framework. However, the code was not successfully run on either PROOF or GRID.

5.4.1 Implemented Algorithm

The first step in the analysis algorithm described in section 4.10 is implemented in an AliAnalysisTaskSE object named AliAnalysisTaskIMCalib. It does the following for each event:

A.1 Recalculate clusters based on current set Calibration Data Base (CDB)

A.2 Discard clusters that do not pass single cluster cuts

A.3 Pair clusters, then:

- A.3.1 Discard pairs of clusters that do not pass two cluster cuts
- A.3.2 Calculate invariant mass
- A.3.3 Fill cell histograms corresponding to the center cells of clusters with the reconstructed IMs

The second step in the analysis algorithm is implemented in an stand alone AliRoot executable. It does the following:

B.1 Take cell histograms with *'sufficient statistics'* and fit them with a Gaussian, plus noise (2 degree polynomial)

B.2 Calculate a new set of CCs using the old set and the fits, using function 4.22 with the mean of the fitted Gaussian as 'm_p'

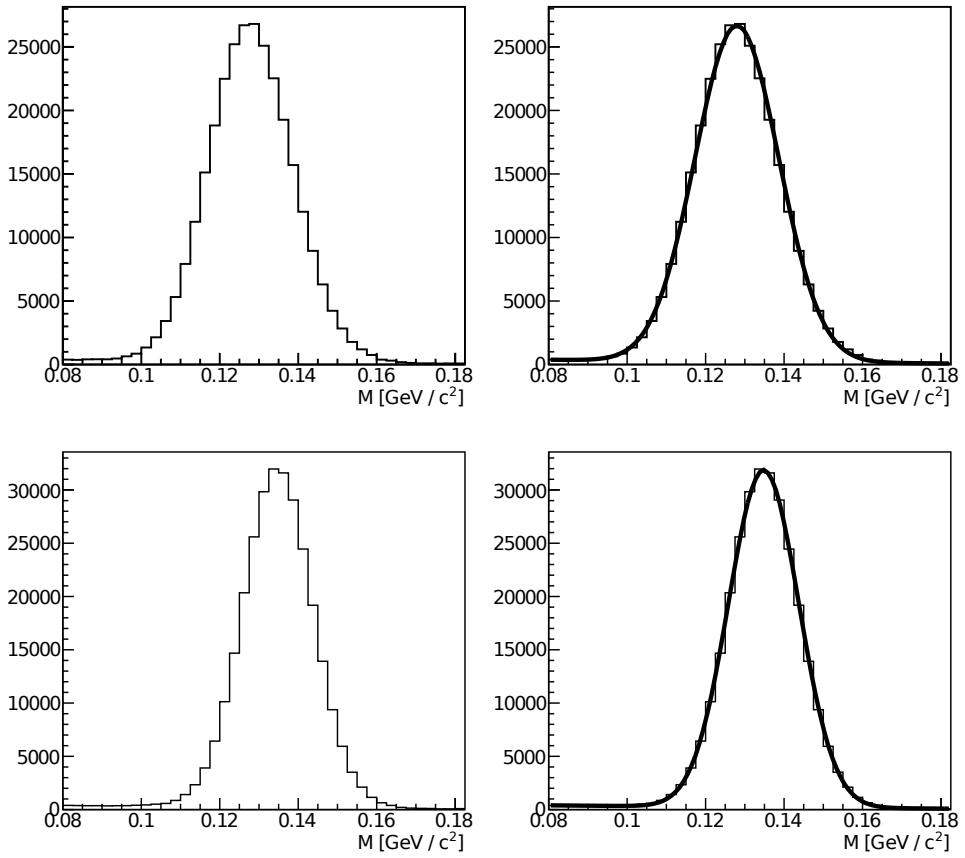

Figure 5.3: π^0 invariant mass plots. The invariant masses of 6×10^5 single 10 GeV π^0 events. After the first part of 1. iteration (upper) and 30. iteration (lower), with a fitted Gaussian (right) and without (left).

Sufficient statistics means that the cell has enough reconstructed IM entries to pass a hard cut. This cut is set to reduce the amount of computing time wasted on fit histograms that does not have enough entries to yield helpful results. Even with the hard cut of $N > 50$ used in the following results, it was found that about $\sim 49\%$ of the fits did not converge, produced some other error, or produced unreasonable fit parameters.

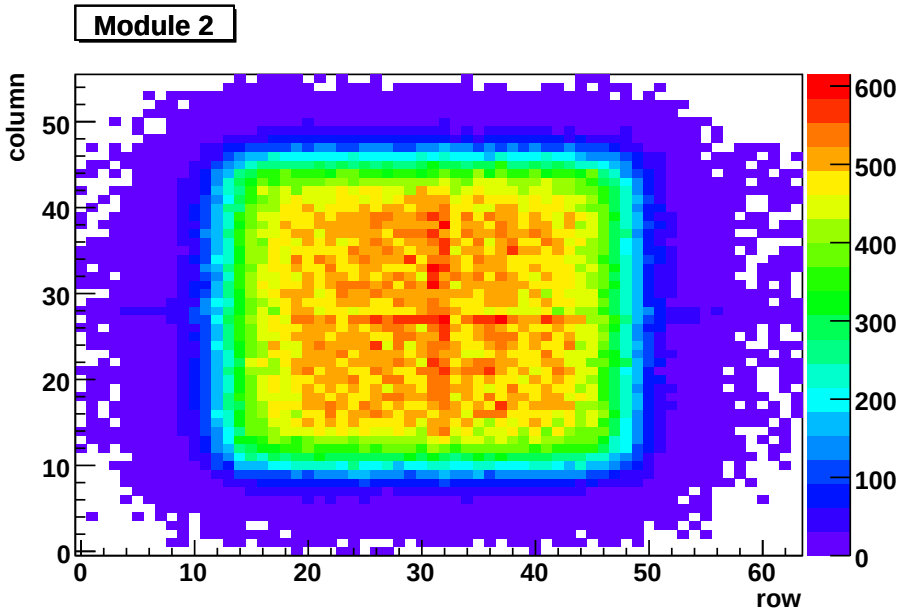

Figure 5.4: Distribution of position of clusters in center module from reconstructed π^0s. Based on 5×10^5 single 10 GeV π^0 events in PHOS, emitted within azimuthal angle x $265° < \phi < 275°$ and angle relative to beam $85° < \theta < 95°$, simulated using geant3 with AliRoot version v4-16-Release.

5.5 Results From Using Single π^0 Events

In ordered to test the algorithm, 3×10^6 events containing a single 10 GeV π^0 were generated using geant3 with AliRoot version v4-16-Release. They were emitted towards a full PHOS setup within an azimuthal angle of $265° < \phi < 275°$ and at an angle relative to the beam axis of $85° < \theta < 95°$.

Due to the limited angles, the center module is not isotropically radiated. The distribution of clusters in the central module is shown in figure 5.4. The limited angles were chosen to achieve a good reconstructable–event over generated–event ratio in order to reduce the amount of events needed, while at the same time spreading the cluster over a wide area of a module.

In all cases a set of 10% decalibrated CCs are used. The CCs were distributed randomly using a Gaussian distribution with $\mu_{CC} = 1$ and $\sigma_{CC} = (\sigma/\mu)_{CC} = 0.1$. The 3×10^6 events were split into sets of $2 - 6 \times 10^5$ events.

5.5.1 3×10^5 Events Calibration Run

In figure 5.5 we see the π^0 IM peak width and position plotted against iterations of the algorithm applied to a data set of $3 \cdot 10^5$ ($\bullet/\circ$) and $1 \cdot 10^5$ ($\diamond$) single 10 GeV π^0 events. In figure 5.6 we see the calibrated CC RMS against iterations. Calibrated CCs are those CCs that corresponds to cells that have sufficient statistics ($N > 50$).

The peak positions starts of at about $\simeq 95\%$ of the ideal position (m_{π^0}) and rises to above 99% within 3 iterations. After this, the positions seems to converge towards the π^0 mass or some value close to it. The widths decreases sharply the first 10 iterations. After this, they seems to converge. We observer that the algorithm using the linear equation ($4.21 : \bullet$) seems to converge faster then using of the alternative equation ($4.22 : \circ$). Also, there seems to be a difference in the values they are converging towards. However, we will show later that this difference is within a reasonable statistical variance. For the remainder of this chapter we will use the linear equation (4.21).

This shows that the algorithm achieves a better then 10% calibration using a 3×10^5 single 10 GeV pi^0 events. However, the peak width is not as small as predicted by equation 5.6 when compared to the CC RMS. We will address this issue later in section 5.6.

5.5.2 π^0 Per Cell Dependency

In order to predict the degree of calibration that can be expected given a set amount of data, we need to examine the relationship between the measures of calibration[2], and some measure of *amount of data*. A useful measure is the number of physics events. However, our results are from simulated single π^0 events, and the relation between the two is not immediately apparent.

We will in the following discussion use the average reconstructable π^0 entry per cell ($\langle N/cell \rangle$) because it can be calculated in both the case of simulated π^0 and physics events. We take $\langle N/cell \rangle$ to be equal the average IM entry per *calibrated cell* in order to account for the anisotropic distribution of the simulated π^0s, Since PHOS is not isotropically radiated in our single π^0 events, we define *calibrated cells* as cells that have sufficient statistics ($N > 50$).

However, we must be aware that we cannot expect the same level of calibration from the same $\langle N/cell \rangle$ for single π^0 events and physic events. This is because real physics events have background. The background negatively effects the estimation of peak mean in cell IM plots which again negatively effects the calibration.

Because the accuracy in the correction of the calibration (C) of the cells is so strongly dependent on the accuracy of the estimation of the peak mean,

[2] see section 5.1

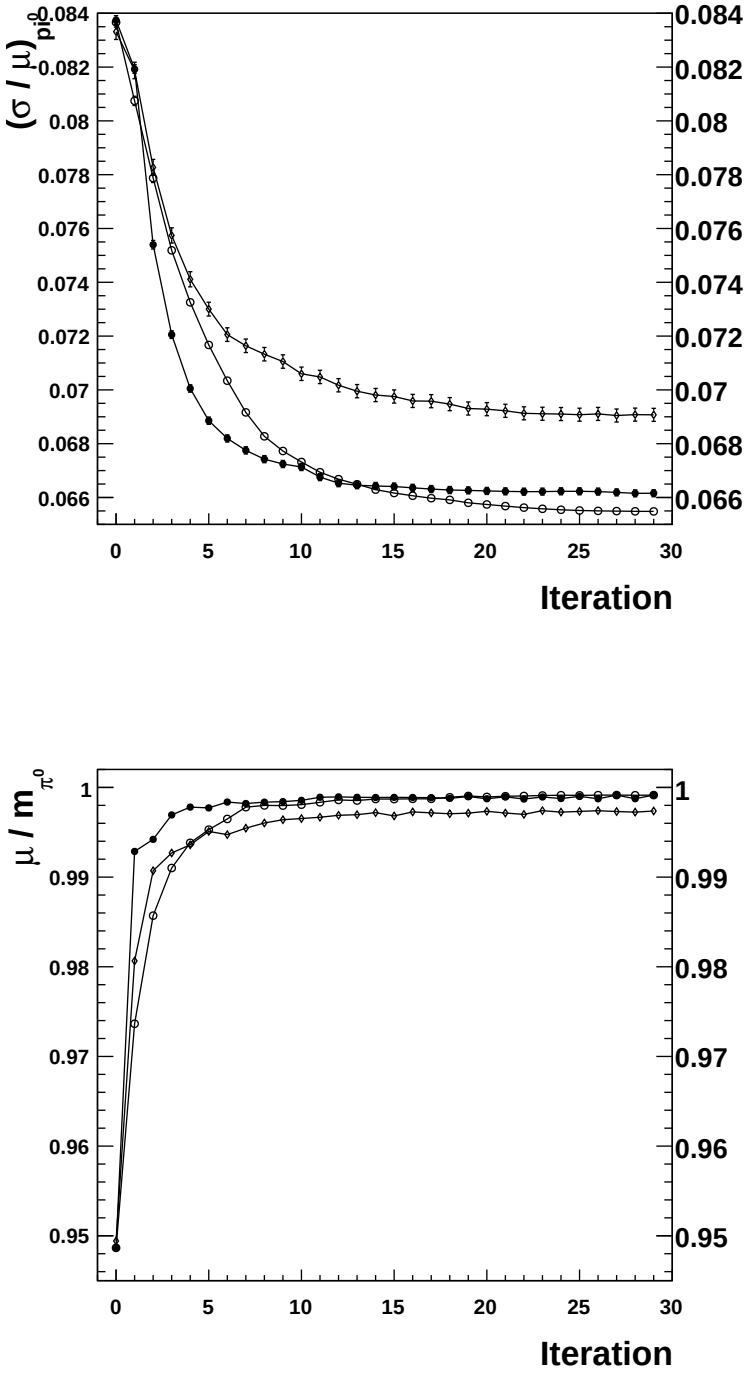

Figure 5.5: π^0 peak width (top) and position (bottom) plotted against iteration. The values are from a run of calibration algorithem using a data set of $3 \cdot 10^5$ single 10 GeV π^0 events using equation 4.21 (•) and 4.22 (○), or $1 \cdot 10^5$ events using equation 4.21 (◇), page 45.

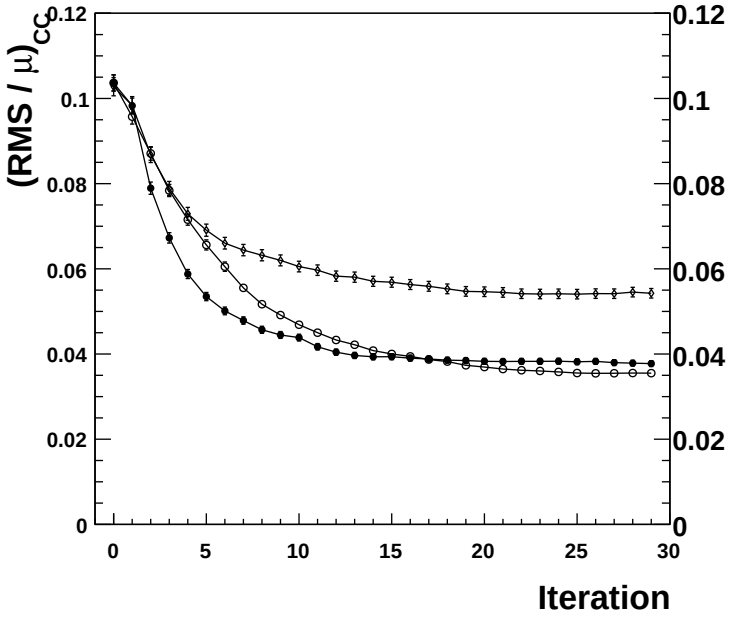

Figure 5.6: *Calibrated* CC RMS ploted against iteration. The values are from a run of calibration algorithem using a data set of $3 \cdot 10^5$ single 10 GeV π^0 events using equation 4.21 (•) and 4.22 (○), or $1 \cdot 10^5$ events using equation 4.21 (◇), page 45.

and the peak mean error ($\sigma_{\hat{mean}}$) can be estimated to be

$$\sigma_{\hat{\mu}} = \frac{\sigma}{\sqrt{N}} \tag{5.8}$$

where N is the sample size. We predict that calibration (C) is to have the following dependence on $\langle\, N/cell \,\rangle$:

$$C \propto \frac{1}{sqrt(\langle\, N/cell \,\rangle)} \tag{5.9}$$

Initial Results

The 6×10^6 single π^0 events were split into smaller sets of $1 - 6 \times 10^5$ events. These sets was applied to the calibration algorithm. The CC RMS corresponding to the smallest reconstructed IM peak width after 30. iterations is plotted against $\langle\, N/cell \,\rangle$ in figure 5.7 for all the sets. The error bars represent the error estimate of the parameters given by the fitting algorithm.

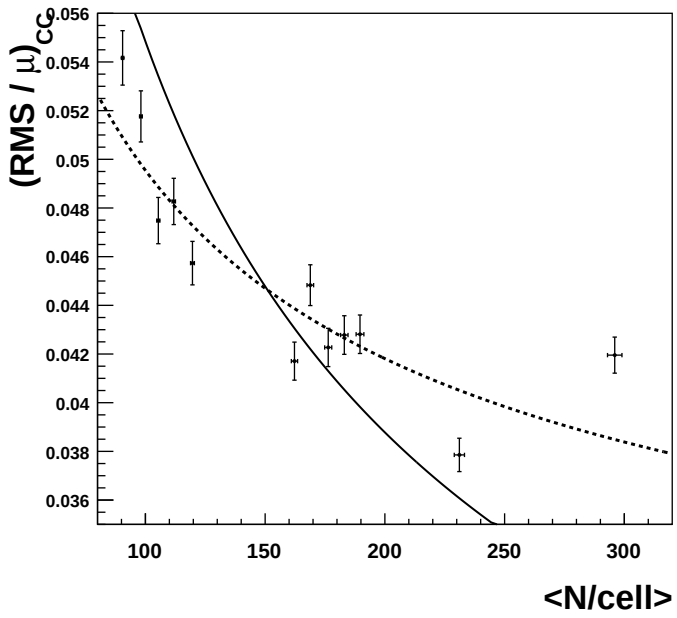

Figure 5.7: The CC RMS corresponding to the smallest reconstructed IM peak width after 30. iterations plotted against $\langle\, N/cell \,\rangle$. The solid line represents a fit to function 5.10, the dashed line represents figure 5.11.

The solid line represents a fit of

$$f_{CC} = \frac{a_0}{\sqrt{\langle\, N/cell \,\rangle}} \tag{5.10}$$

which is accordance with the prediction we made earlier.

The dashed line represents a fit of

$$f'_{CC} = \frac{b_0}{\sqrt{\langle\, N/cell \,\rangle}} + b_1 \tag{5.11}$$

Its pretty clear that measurements do not agree with the prediction. The errors of the measured points are to small. However, it turns out that the errors are under–estimated. We will show that this in the following section.

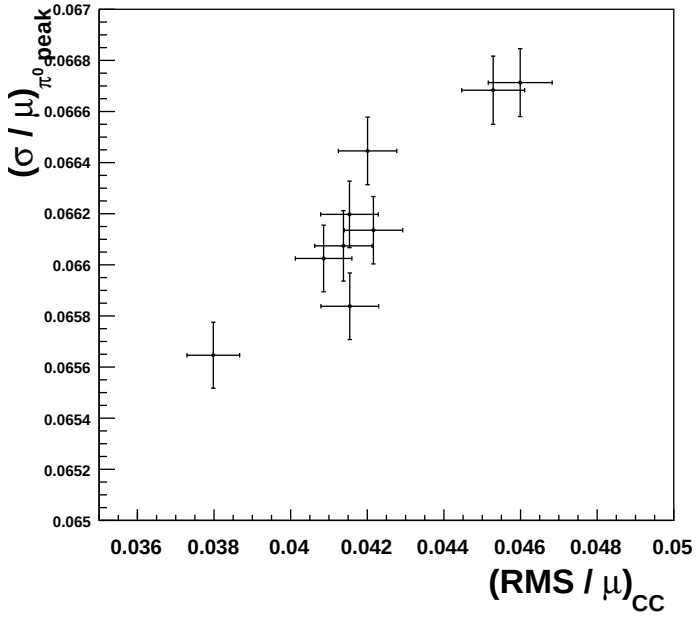

Figure 5.8: The distrobution of the smallest IM peak width after 30. iterations of the calibration algorithem plotted against the corresponding CC RMS. The points are all based on 3×10^5 events, and the error–bars represent the error estimated by the fitting algorithem, clearly to small.

5.5.3 Variance In 3×10^5 Calibration

The 3×10^6 simulated Events were split into 10 sets of 3×10^5 events each. The calibration algorithm was then applied to them. The distribution of the achieved calibration of 9 of these after 30 iterations of the algorithm can be seen in figure 5.8

From the distribution above we can calculate and compare the ratio of the sample standard devotion of $(RMS/\mu)_{CC}$ to the mean of estimated errors of $(RMS/\mu)_{CC}$ calculated by the fitting algorithm

$$\frac{S_{(RMS/\mu)_{CC}}}{\left\langle\ \hat{\sigma}_{(RMS/\mu)_{CC}}\ \right\rangle} = \frac{2.5 \times 10^{-3}}{0.8 \times 10^{-3}} = 3.3 \tag{5.12}$$

and ratio of the sample standard deviation of $(\sigma/\mu)_{\pi^0}$ to the mean of estimated errors of $(\sigma/\mu)_{\pi^0}$ calculated by the fitting algorithm:

$$\frac{S_{(\sigma/\mu)_{\pi^0}}}{\left\langle\ \hat{\sigma}_{(\sigma/\mu)_{\pi^0}}\ \right\rangle} = \frac{3.8 \times 10^{-4}}{1.3 \times 10^{-4}} = 2.9 \tag{5.13}$$

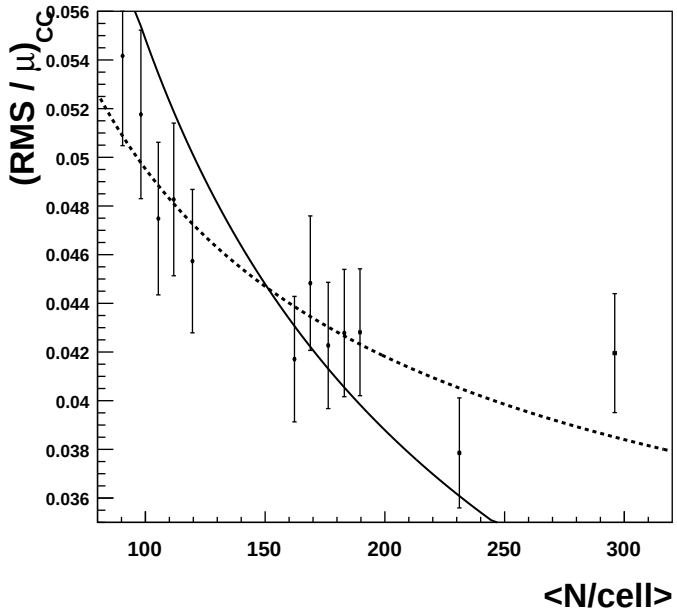

Figure 5.9: The CC RMS corresponding to the smallest reconstructed IM peak width after 30. iterations plotted against $\langle\, N/cell\,\rangle$, with corrected error bars. The solid line represents a fit to function 5.14, the dashed line represents figure 5.15.

This indicates that $\hat{\sigma}_{(RMS/\mu)_{CC}}$ is underestimated by the fitting algorithm by a factor of 3.3, and $\hat{\sigma}_{(\sigma/\mu)_{\pi^0}}$ by a factor of 2.9. We can calculate the same ratio for the average entries per cell, $\hat{\sigma}_{\langle\, N/cell\,\rangle}$, and find it to be 0.21.

Assuming that this ratio is independent on $\langle\, N/cell\,\rangle$, we correct for the underestimation of these errors and plot $(RMS/\mu)_{CC}$ against $\langle\, N/cell\,\rangle$ again in figure 5.9.

5.5.4 CC RMS - π^0 Per Cell Dependency

In figure 5.9, we see $(RMS/\mu)_{CC}$ plotted against $\langle\, N/cell\,\rangle$. The error bars have been scaled with the ratio found in the previous section The solid line represents a fit of:

$$\sigma^0_{CC} = F^0_{CC}(\langle\, N/cell\,\rangle) = \frac{d_0}{\sqrt{\langle\, N/cell\,\rangle}} \tag{5.14}$$

and the dashed line represents a fit of:

$$\sigma_{CC}^{e_1} = F_{CC}^{e_1}(\langle\, N/cell \,\rangle) = \frac{e_0}{\sqrt{\langle\, N/cell \,\rangle}} + e_1 \tag{5.15}$$

d_0	=	$5.49(10) \times 10^{-1}$
e_0	=	$2.63(59) \times 10^{-1}$
e_1	=	$2.32(47) \times 10^{-2}$

Table 5.2: Parameters of function 5.14, and 5.15 fitted to figure 5.9.

The first function (5.14) was what we expected from the argument in the beginning of the section (5.5.2), that the calibration (C) is proportional to $C \propto \frac{d_0}{\sqrt{\langle\, N/cell \,\rangle}}$. The second function (5.15) assumes the same, only that 'C' it converges towards some other value above $C = 0$ ($C \propto \frac{e_0}{\sqrt{\langle\, N/cell \,\rangle}} + e_1$).

It seems that the second function is in better agreement with the results then the first. We can interpret this in two ways. Either the calibration is somehow limited by some lower bound close to $e_1 \simeq 2.32(59)\%$ calibration, or the anisotropic π^0 distribution somehow limits the calibration algorithm from reaching ideal calibration.

5.5.5 Peak Width - π^0 Per Cell Dependency

In figure 5.10, we see $(\sigma/\mu)_{\pi^0}$ plotted against $\langle\, N/cell \,\rangle$. The solid line represents a fit of

$$F_{\pi^0}^0 = c_2 \cdot (\sigma_{CC}^{c_0})^2 + c_1 \cdot (\sigma_{CC}^{c_0}) + c_0 \tag{5.16}$$

where

$$\sigma_{CC}^{c_0}(\langle\, N/cell \,\rangle) = \frac{g_0}{\sqrt{\langle\, N/cell \,\rangle}} \tag{5.17}$$

The dashed line represents a fit of

$$F_{\pi^0}^{h_1} = c_2 \cdot (\sigma_{CC}^{h_1})^2 + c_1 \cdot (\sigma_{CC}^{h_1}) + c_0 \tag{5.18}$$

were

$$\sigma_{CC}^{h_1}(\langle\, N/cell \,\rangle) = \frac{h_0}{\sqrt{\langle\, N/cell \,\rangle}} + h_1 \tag{5.19}$$

The coefficients $\{c_2, c_1, c_0\}$ are these from equation 5.6 fitted to figure 5.2. They can be found in table 5.1 page 52.

The second function seems to be in much better agreement with the results then the first. We can interpret this in the same way as we did the CC RMS against entries plot. Either the anisotropic π^0 distribution somehow limits the calibration, or the calibration is somehow limited by some lower bound, in this case $h_1 = 5.54(3)\%$.

g_0	=	$8.95(7) \times 10^{-1}$
h_0	=	$2.10(41) \times 10^{-1}$
h_1	=	$5.54(3) \times 10^{-2}$

Table 5.3: Parameters of function 5.16, and 5.18 fitted to figure 5.10.

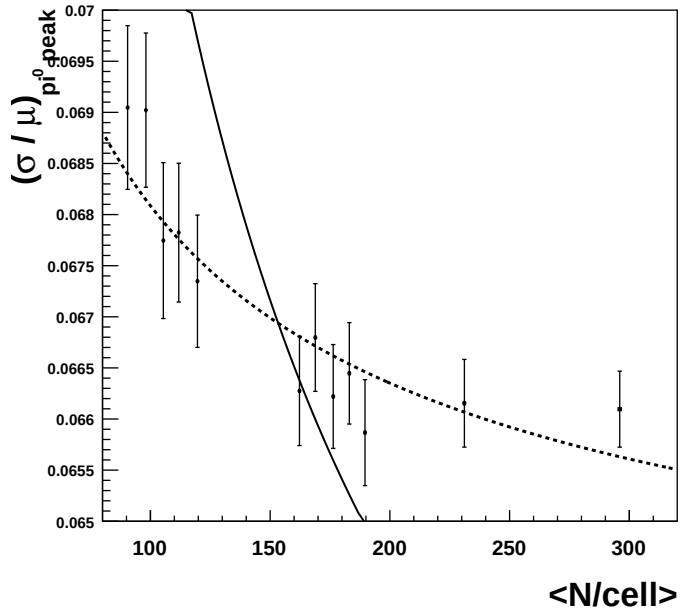

Figure 5.10: The smallest reconstructed IM peak width after 30. iterations plotted against $\langle\, N/cell \,\rangle$. The solid line represents a fit to function 5.16, and the dotted line to function 5.18.

However, the calibration level that the peak width is convergent towards ($h_1 = 5.54(3)\%$) is severely worse then the level the CCs are ($e_1 = 2.32(59)\%$). This raises the question: "Does the relationship between the reconstructed IM peak width and CC RMS follow the prediction from section 5.3?"

5.5.6 Post–Calibration π^0 Peak Calibration Dependency

Before we can interpret these results, we need to address the issue raised in the previous section. "Does the relationship between the reconstructed IM peak width and CC RMS follow the prediction from section 5.3?" In figure 5.11 we see the two plotted against each other. The solid line represent the prediction formulated in equation 5.6) seen in figure 5.2,

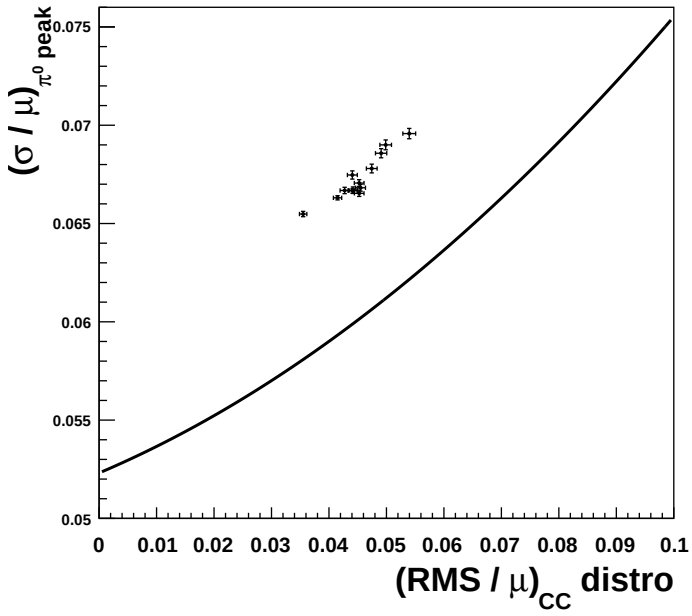

Figure 5.11: The smallest IM peak width after 30. iterations of the calibration algorithem plotted against the corresponding CC RMS. The solid curve is equation 5.6, the relationship between the two predicted in section 5.3.

It is clear from the plot that the points do not follow the prediction. Considering that the algorithm optimises the peak width by peak positions, not CCs, it is surprising that the points are offset to above the line and not to below it. However, it can be explained by considering how the two values are calculated and what set of data points they are based on.

The CC RMS is calculated by taking the RMS of all the CCs that had sufficient statistics. This means that only the CCs that were calibrated were included. In contrast, the IM peak is calculated by fitting a Gaussian distribution to all the reconstructed IMs.

If all the calibration coefficients were calibrated, then the IM peak width would be calculated on the basis of only fully calibrate reconstructed IMs. However, since PHOS is anisotropically radiated, not all cells have sufficient statistics, and a sub–set of the reconstructed IMs are only partially–calibrated or even un–calibrated. In addition, since the un–calibrated IMs are biased towards lower[3] then the π^0 mass values, the calibrated IMs would be biased towards higher then π^0 mass values because the algorithm is trying to optimise the peak position (average) so that it is equal the π^0 mass.

[3]Lower because the initial state of CCs is biased towards lower values, see section 5.3.

This would cause the Gaussian fit to be fitted onto the continuous sum of Gaussian–like peak distributions: ranging from un–calibrated *to* calibrated, wide *to* narrow, and biased towards a lower value *to* biased towards higher then π^0 mass values. Compared to the fully calibrated IMs, the total distribution of the peak would be wider if it includes all the reconstructed IMs.

Assuming that this is not a insignificant effect, it would cause the points in figure 5.11 to be shifted towards a higher $(\sigma/\mu)_{\pi^0 peak}$ and would explain why they are above the expected value.

5.6 Interpretation

In this section we interpret the results. Firstly, its clear that calibration technique achieves a better then 10% calibration with as little as 100 entries per cell. However, the degree of calibration is open to interpretation.

The assumption stated in equation 5.9, does not agree with the results unless we allow the calibration to level out before ideal calibration, i.e:

$$C \propto \frac{1}{\langle\, N/cell \,\rangle} + k \tag{5.20}$$

where 'k' is a constant representing a lower limit of the calibration.

If we use the CC RMS as a measure of calibration, we find that 'k' is equal to:

$$k_{CC} = e_1 = 2.32(47)\% \tag{5.21}$$

If we use the π^0 peak width as a measure of calibration, we find that 'k' is equal to;

$$k_{\sigma_{\pi^0}} = h_1 = 5.54(3)\% \tag{5.22}$$

however, we have argued in section 5.5.6 that the calibration level calculated by using the π^0 peak width will be artificially high.

This can be interpreted in two extremes:

'A' The calibration levels of at 'k'. This is the best achievable calibration achievable using the π^0 IM calibration technique.

'B' The calibration levels of at 'k' if we interpolate from the measured range ($< N/cell > \simeq (100, 300)$). However, this is a effect of the anisotropic distribution of the π^0s, and using a isotropic distribution would cause the calibration to level of at 0.

Due to the anisotropic distribution of π^0, the reconstructable π^0 cluster pair clusters are not distributed evenly across PHOS cells. The distribution can be seen in figure 5.4 on page 55 for a set of 5×10^5 single π^0 events. We see the distribution of entries per cell in figure 5.12 for 9 3×10^5 events.

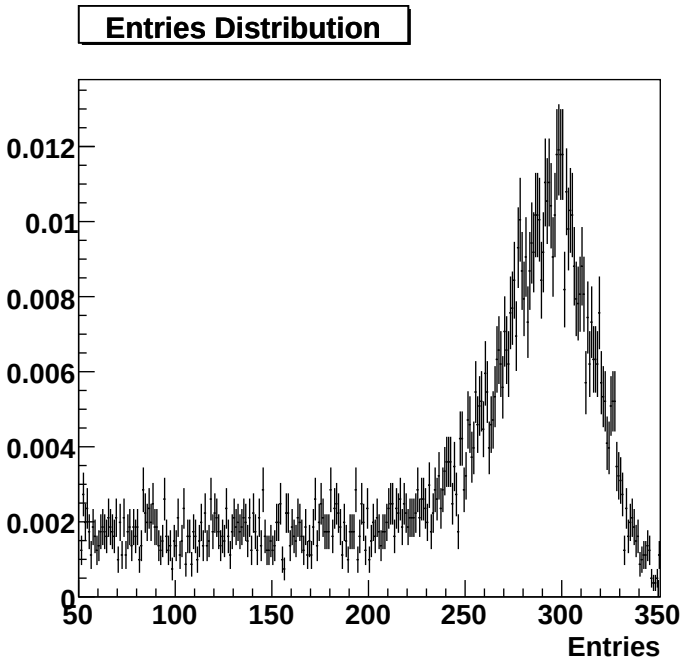

Figure 5.12: Distribution of position of clusters in center module from reconstructed π^0s. Based on 9 3×10^5 single 10 GeV π^0 events in PHOS, emitted within azimuthal angle x $265^\circ < \phi < 275^\circ$ and angle relative to beam $85^\circ < \theta < 95^\circ$, simulated using geant3 with AliRoot version v4-16-Release.

Analogous to how the π^0 peak width is overestimated due to un–calibrated reconstructed π^0s, the CC RMS is also arguably overestimated. The distribution of entries per cell is not symmetric around its mean. It has a tail at low entries. This tail will cause $< N/cell >$ to be shifted towards lower values. However, it will also cause the CC RMS to increase and the CC mean to decrease.

Assuming that this is not a insignificant effect. The question becomes, "how do we estimate the expected level of calibration of a isotropic distribution as a function of $< N/cell >$?" If we assume that the overestimation of calibration (σ_{CC}) is independent of $< N/cell >$ in the range of ($< N/cell > \simeq (100, 300)$, and that the calibration should converge as

$$C \propto \frac{1}{\sqrt{\langle N/cell \rangle}}$$

then the calibration would be

$$\sigma_{CC}^{\not e_1} = \sigma_{CC}^{e_1} - e_1 = \frac{e_0}{\sqrt{\langle\, N/cell \,\rangle}} \tag{5.23}$$

Assuming that the fit of equation 5.15 is a accurate description of the calibration dependency on $< N/cell >$, and that the calibration is limited by e_1, equation 5.15 again:

$$\sigma_{CC}^{e_1} == \frac{e_0}{\sqrt{\langle\, N/cell \,\rangle}} + e_1$$

5.6.1 p–p Collisions

In this section we will try and connect the results with p–p collisions. In section 4.7.2 we found that a p–p collision produces at average $\frac{N_{\pi^0}}{N_{p-p}} = 0.0152(2)$ reconstructable π^0, given a π^0 $p_T > 1\ GeV$ cut.

The maximum ALICE p–p luminosity is[10]:

$$\mathcal{L}_{high} = 5 \times 10^{30} cm^{-1} s^{-1} \tag{5.24}$$

which corresponds to a interaction rate of 200 kHz. During 24 hours, this would correspond to 1.7×10^{10} events or $1.47(2) \times 10^4$ reconstructable π^0 per cell. Since a π^0 produces 2 clusters, the number of entries per cell per day would be

$$(< \frac{N}{cell} > /d)_{\mathcal{L}_{high}} = 2.93(4) \times 10^4 \tag{5.25}$$

Using the optimistic interpretation that the offset is independent of $< N/cell >$ in the range of $(< N/cell > \simeq (100, 300)$, then the calibration achieved using the data from 24 hours of running (eq. 5.23 page 67) would be

$$(\sigma_{CC}^{\not e_1})_{\mathcal{L}_{high}} = \frac{e_0}{\sqrt{2.93(4) \times 10^4}} = 0.15(3)\% \tag{5.26}$$

However, this does not take into account the combinatorial background, which will negatively effect the calibration.

Using the pessimistic interpretation that the offset is correct, then the calibration achieved using the data from 24 hours of running (eq. 5.6 page 67) would be

$$(\sigma_{CC}^{e_1})_{\mathcal{L}_{high}} = \frac{e_0}{\sqrt{2.93(4) \times 10^4}} + e_1 = 2.5(5)\% \tag{5.27}$$

which again does not take into account the combinatorial background.

If ALICE runs at the low luminosity $\mathcal{L}_{high} = 1 \times 10^{29} cm^{-1} s^{-1}$, then the calibration achieved from 24 hours of running using the optimistic interpretation would be

$$(\sigma_{CC}^{\not e_1})_{\mathcal{L}_{low}} = 1.1(2)\% \tag{5.28}$$

The amount of data that can be applied to the algorithm is limited by how stable PHOS's gain is. For example, if the APD bias voltage settings are changed, then the algorithm needs to be run separately for the two settings, and the results only have meaning to the corresponding settings. Furthermore, if the gain drift over time, then it might be optimal to segment a large set of data into smaller sets and apply the algorithm separately.

The algorithm is also limited by the fact that it requires such a large amount of data. The current implementation of the algorithm takes ~ 5 hours of computing time to run 30. iteration on 1×10^5 π^0 events. If we scale that with the 1.7×10^{10} p–p events that will be produced in ALICE at high luminosity, then we find that 30 iterations of 24 hours worth of data wold take 8.6×10^5 hours of computing time. This estimate ignores the low production rate of π^0s. However, it does not take into account the combinatorial background either. The take home message is, that the algorithm will have to be optimized and run on the GRID.

Chapter 6

Conclusion

There are various techniques available for calibration of the PHOton Spectrometer (PHOS) at the ALICE heavy ion experiment at CERN.

Charged cosmic muons are Minimum Ionizing Particles, and their predicable deposition of energy can be used as a reference for calibrating PHOS. These cosmic particles are always available, so they provide a source of calibration that can be applied before LHC runs. However, cosmic muons appear at relative low frequency, so the degree of calibration the technique can yield is limited.

Equalisation of gains using total measured energy is a calibration technique that can yield usable calibration results rather quickly. However, it does not provide the required accuracy, so it will not be used as the final calibration technique. LHC collisions provide a large number of pions, and they can be used to calibrate PHOS, much like cosmic muons. These produced pions provide another fast source of calibration, but the degree of calibration they provide is limited by how accurately the energy loss of charged pions can be determined for different momenta.

Lastly, we looked at a calibration technique utilising $\pi^0 \rightarrow \gamma\gamma$ invariant mass reconstruction. The degree of calibration that can be achieved using this technique is limited by the frequency of reconstructable π^0 in PHOS, and on how stable the gain of PHOS is over the time (in the order of hours) needed to accumulate sufficient statistics.

From the results presented in this thesis, it's clear that CC calibration using reconstructed π^0 IMs is viable, but that the technique requires in the order of $\sim 10^9 - 10^{10}$ p–p events. ALICE needs on the scale of $1 - 20$ hours in order to collect this amount of data.

The calibration technique can perform calibration of the CCs to a relative degree of 0.15(3)%, using 24 hours worth of data, provided that the assumption that the offset of CC RMS is independent of $< N/cell >$ in the range of $(< N/cell > \simeq (100, 300)$ is correct. However, this is dependent on the stability of the detectors gains.

The assumption could be tested by simulating isotropically distributed single π^0 events and running the calibration algorithm. If the assumption is correct, then the resulting calibration should match the expectation from equation 5.23 (page 67). This could also be used to test the explanation of the shift seen in section 5.5.6, figure 5.11. Alternatively, p–p events could be used. However, this would require at least a factor of ~ 100 more events.

The technique requires a large amount of data, so the parameters of the algorithm should be optimized. These parameters include the cluster and cluster pair cuts. In addition, the function used to correct the CC using the cell peak position has a large effect on the speed which the calibration converges, and it should also be optimized. This could be accomplished by varying the parameters/function and comparing the results.

In figure 5.1, it is clear that the π^0 peak deviates by $\pm 1\%$. This deviation is probably due to outdated non–linear correction coefficients[23]. However, it might be a good idea to study this deviation since a 2. degree polynomial may not be able to acceptably account for the shape of non–linear effects in PHOS.

Bibliography

[1] W. M. Yao and *et al.* Review of particle physics. *Journal of Physics G: Nuclear and Particle Physics*, 33:1–1232, 2006.

[2] D. J. Gross and F. Wilczek. Ultraviolet behavior of non-abelian gauge theories. *Phys. Rev. Lett.*, 30:1343–1346, 1973.

[3] H. D. Politzer. Reliable perturbative results for strong interactions? *Phys. Rev. Lett.*, 30:1346–1349, 1973.

[4] GSI. The CBM experiment introduction. `http://www.gsi.de/fair/experiments/CBM/1intro_e.html`, 2009.

[5] B. Müller and J. L. Nagle. Results from the relativistic heavy ion collider. *Annual Review of Nuclear and Particle Science*, 56:93–135, 2006.

[6] J. Frantz. Illuminating RHIC matter with the multi-purpose direct photon. *Journal of Physics G: Nuclear and Particle Physics*, 34:S389–S396, 2007.

[7] W R Leo. *Techniques for nuclear and particle physics experiments.* Springer-Verlag, second edition, 1993.

[8] M. Hamann and T. Weaver. Measurement of the energy distribution of particle showers : Theory. `http://mxp.physics.umn.edu/s06/Projects/S06_ParticleShowerEnergy/theory%.htm`, 2009.

[9] ALICE Collaboration, B. Alessandro, F. Antinori, J. A. Belikov, and *et al.* ALICE: physics performance report, Volume II. *Journal of Physics G: Nuclear and Particle Physics*, 32:1295–2040, 2006.

[10] ALICE Collaboration, F. Carminati, P. Foka, P. Giubellino, and *et al.* ALICE: physics performance report, Volume I. *Journal of Physics G: Nuclear and Particle Physics*, 30:1517–1763, 2004.

[11] T. Cormier, C. W. Fabjan, L. Riccati, and H. de Groot. Alice electromagnetic calorimeter: addendum to the ALICE technical proposal.

CERN Document Server, (CERN-LHCC-2006-014. CERN-LHCC-96-32-ADD-3), 2006.

[12] C. W. Fabjan, L Jirdén, V Lindestruth, L. Riccati, D Rorich, P. Van de Vyvre, and *et al.* Alice trigger data-acquisition high-level trigger and control system: Technical design report. *CERN Document Server*, (CERN-LHCC-2003-062), 2004.

[13] The ALICE Collaboration, K Aamodt, and *et al.* The ALICE experiment at the CERN LHC. *Journal of Instrumentation*, 3:S08002, 2008.

[14] ALICE Collaboration and *et al.* Alice: Technical proposal for a large ion collider experiment at the cern lhc. *CERN Document Server*, (CERN-LHCC-95-71), 1995.

[15] D C Zhou (for the ALICE Collaboration). PHOS, the ALICE-PHOton spectrometer. *Journal of Physics G: Nuclear and Particle Physics*, 34:S719–S723, 2007.

[16] V I Man'ko, W Klempt, L Leistam, J De Groot, and Jürgen Schükraft. Alice photon spectrometer (phos): Technical design report. *CERN Document Server*, (CERN-LHCC-99-004), 1999.

[17] G Conesa, H Delagrange, J Diaz, D Peressounko, and Y Schutz. Detector performance studies and particle identification with PHOS. CERN Document server, (ALICE-INT-2005-053), 2005.

[18] Eric W Weisstein. "Hadamard Product". From MathWorld–A Wolfram Web Resource. `http://mathworld.wolfram.com/HadamardProduct.html`, 2009.

[19] H. Muller, D. Budnikov, M. Ippolitov, Q. Li, and *et al.* Front-end electronics for PWO-based PHOS calorimeter of ALICE. *Nuclear Instruments and Methods in Physics Research Section A: Accelerators, Spectrometers, Detectors and Associated Equipment*, 567:264 – 267, 2006.

[20] F. Chuman, A. Hiei, T.C Horaguchi, Kenta Mizoguchi, and *et al.* Calibration methods of PHOS modules. Under Review: CERN Internal Note/ALICE-INT-2008-xxx, 2008.

[21] Yuri Kharlov. Personal correspondence.

[22] Boris Polichtchouk. Personal correspondence.

[23] Torii Hisayuki. Personal correspondence.

[24] Y. Kharlov, B. Polichtchouk, H. Torii, and Y. Mao. CERN Indico: PHOS analysis Task Force meeting. `http://indico.cern.ch/conferenceDisplay.py?confId=36806`.